# Sex-dependent impairments of parvalbumin expressing neurons in the retrosplenial cortex in Alzheimer's disease

**Dylan J. Terstege[1,2], Yi Ren[1,2], Derya Sargin[2,3,4], Jonathan R. Epp[1,2*]**

[1] Department of Cell Biology and Anatomy, Cumming School of Medicine, University of Calgary, Canada; [2] Hotchkiss Brain Institute, University of Calgary, Canada; [3] Department of Psychology, University of Calgary, Canada; [4] Alberta Children's Hospital Research Institute, University of Calgary, Canada

* Correspondence:
Jonathan R. Epp
Jonathan.Epp1@UCalgary.ca

## Abstract

**Alzheimer's Disease is a common and debilitating neurodegenerative disorder with no cure and few treatment options. Impaired metabolism in the retrosplenial cortex during prodromal stages of the disease has been proposed as a strong predictor of future cognitive impairments. The retrosplenial cortex is also one of the earliest brain regions to exhibit functional impairments in Alzheimer's Disease. Therefore, understanding Alzheimer's related deficits in the retrosplenial cortex may be critical in understanding the origins of cognitive impairment and could provide early treatment targets. Here, we investigated alterations in retrosplenial cortex structure and function in a mouse model of Alzheimer's Disease. We identified a novel sex dependent early impairment in parvalbumin-interneuron activity which, is sufficient to induce cognitive impairments and, dysregulate functional connectivity of the retrosplenial cortex. Reversal of cognitive deficits by stimulation of parvalbumin interneurons in retrosplenial cortex suggests that this may serve as a promising novel therapeutic strategy.**

## Main

Alzheimer's disease (AD) is associated with hallmark pathological changes in the brain typically including progressive appearance of amyloid plaques and neurofibrillary tangles. Even prior to the development of these pathological markers, numerous changes can be identified in brain structure and function. One of the earliest observed functional changes in individuals with mild cognitive impairment, who later go on to develop AD, is the development of hypometabolism in the posterior cingulate and especially the retrosplenial cortex (RSC)[1–3]. This early observation can occur years prior to the onset of AD and the degree of metabolic impairment may even predict the rate of conversion from mild cognitive impairment (MCI) to AD[4]. Understanding the changes that occur in the RSC in AD and how they lead to cognitive impairments may provide critical insight into AD progression. There is currently little known about the sorts of structural and functional changes that occur in the RSC. Previous work has shown however, that the RSC is a highly interconnected brain region which is critical for numerous forms of cognition[5–7]. This, in conjunction with the early impairments in the RSC, warrant further investigation.

In the current study we performed an in-depth analysis of the RSC in the context of AD using a transgenic mouse model. We demonstrate here that the activity of the RSC is disrupted in 5xFAD mice. Our results point to impaired inhibition due to a significant dysregulation of fast-spiking parvalbumin interneuron (PV-INs) and a selective vulnerability to loss of PV-INs, which we further confirmed in human AD tissue. As a consequence of this impaired inhibition, there is a disruption of global functional connectivity and cognitive performance. Chemogenetic stimulation of the remaining PV-INs is sufficient to re-establish normal patterns of functional connectivity and enhance memory performance. Importantly, we found that the PV-IN impairments occur to a greater extent and begin earlier in females compared to males. This difference may help to explain the earlier onset of cognitive impairments in females with AD.

## Results

### Activity changes in the RSC of 5xFAD mice.

The clinical observation of hypometabolic function in the RSC is intriguing because it occurs extremely early in the pathogenesis of AD/MCI[4]. To explore the functional implications of this hypometabolism we first confirmed that disrupted metabolic activity is observed in the RSC of 5xFAD mice (Fig. 1a-d). Using the general metabolic label cytochrome C oxidase, we found that there was a reduction in the metabolic activity of the RSC of female, but not male, 5xFAD mice (Fig. 1c). We found the same sex dependent difference when we examined the neuronal glucose transporter GLUT3 in the RSC (Fig. 1d). These data show that in middle aged 5xFAD mice, females but not males exhibit 'early' hypometabolism in the RSC. In contrast, we observed comparable amyloid pathology in the RSC of female and male 5xFAD mice (Extended Data Fig. 1)[8].

Hypometabolism and neuronal hyperexcitability are often closely linked and, hyperactivity in the RSC of AD patients has been observed in fMRI studies[9,10]. Because of this, we predicted an increase in excitability of the RSC of 5xFAD mice. Using c-Fos immunohistochemistry following contextual fear conditioning we determined that there is an increase in the number of active neurons in the RSC of female, but not male 5xFAD mice, suggesting that there is a sex-dependent increase in excitability in the RSC (Fig. 1e,f). To further investigate excitability differences, we used whole-cell patch clamp electrophysiology to quantify activity changes in excitatory and inhibitory cells of 5xFAD mice. In response to depolarizing current input, the excitatory pyramidal neurons in the RSC of female 5xFAD mice fired at a significantly greater frequency, compared to WT mice (Fig. 2a-f). While there was a small but significant increase in the excitability of RSC pyramidal cells in male 5xFAD mice, the effect was consistently larger at all current steps in female 5xFAD mice compared to WT. With the exception of a decrease in the capacitance in female 5xFAD mice there were no differences in any of the measured passive membrane properties of pyramidal cells in female or male 5xFAD mice (Extended Data Fig. 2). Next, we recorded spontaneous inhibitory postsynaptic currents (sIPSC) in pyramidal neurons. We observed a significant decrease in sIPSC amplitude in female but not male 5xFAD mice suggesting a disruption of inhibitory control of pyramidal neurons in the female 5xFAD RSC (Fig. 2g-n).

Parvalbumin-expressing fast-spiking inhibitory interneurons (PV-INs) make up the largest subpopulation of inhibitory neurons in the cortex and as such represent an important mechanism for regulating pyramidal cell excitability[11–13]. To determine whether the increased RSC excitability could relate to impaired PV-IN activity, we examined the electrophysiological properties of the PV-INs in the RSC. To the extent that excitatory neuronal activity was disrupted in 5xFAD mice we predicted an impairment in the activity of PV-INs. Therefore, we expected to observe a greater impairment in female PV-INs in 5xFAD mice. In males, we observed no significant differences in the excitability of PV-INs of 5xFAD mice compared to WT mice (Fig. 2o-r). However, in female 5xFAD mice, we found significant impairments in the activity of PV-INs (Fig. 2s-v). Interestingly, the pattern of impairment across PV-INs was not homogeneous. Instead, we observed two discrete populations based on their activity profiles across the I/O curve (Fig 2u). One population of PV-INs which we have termed “impaired” accounted for approximately half of the recorded neurons. These cells exhibited significantly elevated firing frequency at low depolarizing current inputs but then enter a state of depolarization block in response to larger current inputs (> 250 pA). In contrast, the other population termed “normal” exhibited normal firing frequencies at all depolarizing current inputs (Fig. 2v). We identified further differences in some passive membrane properties of PV-INs (input resistance, capacitance, rheobase current), which were evident only in the impaired PV-IN population in 5xFAD female (Extended Data Fig. 3). There were no significant differences in the membrane characteristics of the normal PV-IN population of female 5XFAD mice, or PV-INs of male 5XFAD mice, compared with WTs (Extended Data Fig. 3). Although not all PV-INs are affected in 5xFAD female mice, it is evident that there is a broad impairment in the normal activity pattern of these inhibitory interneurons in females that does not occur in the male 5xFAD RSC.

To determine whether differences in PV-IN activity could be observed at the population level *in vivo*, we performed calcium imaging with fiber photometry during a forced alternation variant of the Y-maze (Fig. 3; see Extended Data Fig. 4 for examples of individual photometry traces). To record activity specifically from PV-INs we used an AAV virus with the PV specific promoter S5E2 to express GCaMP6f. Mice were first habituated to two arms of the Y-maze. During the test trial, mice were allowed to explore all three of the arms. We found a significant main effect of genotype on time spent in the novel arm as well as a sex by genotype interaction with a significant decrease in time spent in the novel arm in female (but not male) 5xFAD mice indicating impaired recognition memory (Fig. 3c). *In vivo* fiber photometry in WT mice revealed a typical increase in the PV-IN GCaMP6f population activity during the transition between familiar and novel arms of the Y-maze. However, the magnitude of this signal was significantly reduced in 5xFAD mice (main effect of genotype; Fig. 3d-g). Although there was no significant sex by genotype interaction, we noted that the effect size was larger in females than it was in males. Overall, these data show an impairment in PV-IN activity during behavioral performance. At the population level, PV-IN inhibition is reduced and this finding is particularly robust in female 5xFAD mice.

**Immunohistochemical changes in the expression of PV interneurons in the RSC.**

Given the disrupted activity pattern found in female 5xFAD mice, we next investigated whether there was also a corresponding loss of PV-INs in the RSC (Fig. 4). We performed immunohistochemical labeling for parvalbumin and observed a significant loss in the number of PV-INs in the RSC of 6-month old female 5xFAD mice compared to WTs (Fig. 4a,b). In age-matched males however, there was no difference between WT and 5xFAD mice. These data are in agreement with our electrophysiological findings which suggest that the PV-IN vulnerability is sexually divergent. We sought to establish that this result was not an attribute specific to the 5xFAD transgenic line but one that can be generalized as an AD-related phenotype. Further investigation of the TgCRDN8 model of AD revealed the same pattern of early RSC PV-IN loss in female but not male TG+ mice, compared to WTs (Extended Data Fig. 5)[14].

The loss of PV-INs has been reported in numerous brain regions of AD patients and transgenic AD mice in prior studies[15,16]. Therefore, we also investigated whether the magnitude and time course of loss of PV-INs could be recapitulated in other brain regions that show early pathology in AD. To address this, we quantified PV-INs in the entorhinal cortex, subiculum, CA1 of the hippocampus of 5xFAD mice[17]. Visual cortex was also included as it borders the RSC in the mouse brain. In 6-month-old 5xFAD and WT mice, we found that the number of PV-INs was comparable in the additional brain regions investigated (Extended Data Fig. 6). Interestingly, in all regions there was a significant main effect of sex demonstrating that females, regardless of genotype, have fewer PV-INs than males. To determine whether there is an eventual loss of PV-INs in these brain regions, we examined 5XFAD mice at the age of 12 months. At advanced age, we detected significant reductions in the number of PV-INs in 5xFAD mice regardless of sex. These data revealed that the loss of PV-INs is not selective as AD progresses but, that there is an earlier loss of PV neurons specifically in the female RSC in comparison to males and, in comparison to other brain regions.

To distinguish whether the loss of PV-INs in the RSC of 6-month-old female 5xFAD mice is a result of a generalized increase in neuronal death or specific to PV-INs, we quantified the pan-neuronal marker NeuN (Fig. 4d-f). In stark contrast to the approximate 40% loss of PV-INs in female mice, the overall decrease in RSC neurons amounted to only 6% in females. This suggests that the PV-INs in the female RSC are exceptionally vulnerable both in comparison to other neuron types in the RSC or to PV-INs in other brain regions. At an older age (12-months old), the percent loss of RSC PV-INs in 5xFAD males and females was comparable (38% and 43% respectively). The 12-month-old male and female 5xFAD mice had a 17% and 20% reduction in NeuN labeling respectively. These data show that even at an advanced stage, the loss of PV-INs remains disproportionate compared to overall neuronal loss.

A predicted corollary of a decrease in the number of PV-INs in the female 5xFAD mice is that the number of synaptic contacts originating from PV-INs should also decrease. Using immunohistochemistry for synaptotagmin-2 (SYT2) a presynaptic marker which is highly selective for PV-INs (Extended Data Fig. 7c,d), we quantified the total number of presynaptic PV-IN terminals in the RSC (Fig. 4g,h). We also quantified the number of SYT2 puncta surrounding CaMKII-labelled neurons (largely excitatory) as well as those surrounding other RSC PV-INs. We found a significant decrease in the overall density of SYT2 labeling in the RSC only in female but not male 5xFAD mice. Further investigation of cell type specific changes in SYT2 labeling revealed a significant decrease in the number of SYT2 presynaptic terminals contacting CaMKII neurons (Fig. 4i,j) and a smaller, but still significant, difference in the number of SYT2 puncta on PV-IN cell bodies (Fig. 4k,l). These findings suggest a preferential reduction in the inhibition of excitatory neurons in female 5xFAD mice. This corroborates our electrophysiological findings showing hyperexcitability of RSC pyramidal neurons in female 5xFAD mice.

**Validation of PV interneuron deficits as a factor in AD.**

Previous studies have reported a reduction in the number of inhibitory interneurons in human post-mortem hippocampal tissue[18,19]. However, to our knowledge, this has not been investigated in the human RSC. In order to ensure that the loss of PV interneurons in the 5xFAD (and CRND8) mice is representative of the pattern of cell loss that is observed clinically in AD patients, we obtained post-mortem tissue samples to quantify PV-IN expression in the RSC (i.e., Broadman's area 29/30). Tissue blocks were obtained from female and male subjects diagnosed with AD or non-demented, age-matched controls. Labeling of the tissue for parvalbumin demonstrated that AD patients have a significant decrease in the number of PV-INs in the RSC compared to controls (Fig 5). Moreover, female controls had significantly fewer PV-INs compared to male controls, replicating the baseline sex difference that we observed in mice (Extended Data Fig. 6a,b).

**Cognitive impairments and network abnormalities in 5xFAD mice.**

Together our data show that female 5xFAD mice exhibit severe disruptions in the expression, connectivity, and the activity of PV-INs in the RSC. The RSC itself has been implicated in numerous forms of learning and memory with a particular regard for tasks that involve spatial and contextual components. In particular, deficits have been observed in object/location memory tasks, spatial working memory, and contextual memory retrieval following RSC damage[20–22].

Regardless of sex, 5xFAD mice showed significant impairments in an object-location task and a contextual fear conditioning task (Fig. 6a-d). Similar to what we observed with the forced alternation task, there were no significant sex by genotype interactions, but the effect size of cognitive impairments was greater in female 5xFAD mice compared to males in all behavioral tests.

Our results to this point clearly indicate that there are localized impairments in the activity of the RSC. However, the RSC also exhibits extensive structural and functional connectivity with numerous other brain regions implicated in cognition and memory processes. The impact of disrupted RSC PV-IN activity is highly likely to ultimately disrupt communication with other brain regions. Therefore, we investigated whether there were differences in the functional connectivity of the RSC in 5xFAD mice, compared with controls using a brain-wide c-Fos based approach (Fig. 6e). Mice underwent contextual fear conditioning and 24 hours later they were given a 5-minute retention test. 90 minutes after testing, mice were perfused. We used c-Fos immunolabelling to quantify regional activity across the brain during the contextual memory retention test. The RSC was used as a seed to examine functional connectivity between 90 brain regions (i.e., correlated regional activity) (Fig. 6e-i). We assessed a number of graph theory metrics (e.g., local efficiency, betweenness centrality; Extended Data Fig. 8) to understand the potential changes in the functional connectivity of the RSC. A striking difference that emerged was a substantial increase in anti-correlated activity between the RSC and other brain regions. While the number of anti-correlated functional connections is typically quite low in control groups, these were substantially increased in female 5xFAD mice (Fig. 6j). Male 5xFAD mice did not show the same increase; and instead show a small decrease in the number of anti-correlated connections (Fig. 6k).

The increase in anti-correlated activity of the RSC in female 5xFAD mice is intriguing because it suggests a dysregulation of communication between the RSC and other brain regions that may underlie the observed cognitive impairments[23]. In fact, intact functional connectivity of the RSC has been suggested to be a key indicator of healthy cognitive aging[5]. While anti-correlated activity is often overlooked in functional connectivity studies, it has been speculated that it may relate to activity driven by inhibitory interneurons[24,25]. If so, changes in anti-correlated activity would be predicted to occur based on the loss and disruption of PV-IN activity observed here. To our knowledge, the relationship between local inhibition and anti-correlated functional connectivity has never been directly investigated.

As a test of this relationship, we performed targeted inhibition of PV-INs in the RSC of healthy WT mice (Fig. 7). We infected PV-INs with an AAV expressing the inhibitory chemogenetic DREADD, hM4Di under control of the S5E2 promoter that is highly selective for PV-INs (Extended Data Fig. 9). We predicted that chemogenetic inhibition of PV-INs would impair performance on learning and memory tasks and, would reproduce the pattern of increased RSC anti-correlated functional connectivity that is observed in 5xFAD mice. We found that mice expressing hM4Di in PV-INs and treated with the ligand DCZ, showed significantly weaker contextual fear memory retention compared to mice infected with a control virus (Fig.

7c,d). This was true regardless of sex with an equal effect size observed in female and male mice. The lack of a sex difference in this experiment is not unexpected given that we experimentally induced the underlying impairment in PV-IN activity in both male and female mice. We next perfused the mice 90 minutes following the memory retrieval session to examine functional connectivity (Fig. 7f,g). Mice expressing hM4Di and treated with DCZ displayed increased anti-correlated connectivity (Fig. 7h) as well as a decrease in the local efficiency of the RSC (Extended Data Fig. 9), similar to the observed deficits in female 5xFAD mice. These results demonstrate that the occurrence of increased anti-correlated activity is related to a disruption in PV-IN function. Importantly, these data show that impaired PV-IN activity is sufficient to induce the pattern of functional connectivity observed in 5xFAD mice and the predicted impairment in memory retrieval.

**Stimulation of RSC PV interneurons promotes recovery of function in 5xFAD mice.**

Given the deficits in PV-IN function and the corresponding hyperexcitability of pyramidal neurons, we next explored the use of targeted PV-IN stimulation to rescue behavioral impairments (Fig. 8). We used an AAV expressing the excitatory DREADD hM3Dq under the S5E2 promoter to target PV-INs in the RSC of 6-month-old 5xFAD mice (Fig. 8a). Three weeks after surgery, we performed several behavioral tests to assess whether stimulation of the PV-IN population in the RSC would improve cognitive behavior (Fig. 8b). The DREADD agonist DCZ was administered prior to performing forced alternation in a Y-maze, and before the retention test of a contextual fear conditioning task. RSC PV-IN stimulation had no effect on behavior in male mice, but led to increased recognition of the novel arm in the Y-maze forced alternation test in female 5xFAD mice (Fig. 8c,d). Contextual fear memory performance was not impacted by RSC PV-IN stimulation in male mice, however, acute DCZ administration improved contextual memory performance in female 5xFAD (Fig. 8e,f). At the cellular level, compared to saline treatment DCZ increased the activity of S5E2-AAV labeled PV-INs as determined by c-Fos colocalization (Extended Data Fig. 10f,g). There was also a corresponding decrease in overall RSC c-Fos expression indicating that the DREADD/DCZ stimulation of PV-IN successfully reduced the hyperexcitability of the region as a whole (Extended Data Fig. 10h,i).

## Discussion

Previous neuroimaging studies have identified alterations in metabolic function in the RSC years prior to the onset of cognitive impairments[1,4]. This makes the RSC one of, if not the earliest region to exhibit Alzheimer's related pathological changes. Additional work has also demonstrated that the degree of metabolic impairment in the RSC is a reliable predictor of conversion from prodromal phase to Alzheimer's disease[26]. More recent fMRI studies have also suggested that the RSC exhibits increased excitability during cognitive processing[9]. Despite these early regional functional impairments in the RSC, little work has been done to characterize the cellular or pathological changes or investigate the implications for cognitive performance. The RSC itself is critical for a variety of cognitive functions both due to its intrinsic processing as well as its high degree of connectivity with other regions critical for cognition. Understanding the vulnerability of this region to AD-related pathology would be highly beneficial for early diagnostic and/or

intervention strategies. Furthermore, given that there are sex differences in the onset of cognitive impairments in AD, we reasoned that understanding sexually divergent cognitive impairments necessitates examining the earliest impacted brain regions[27–30]. Our goal in the current study was to explore the functional deficits in the female and male RSC using a mouse model of AD. As the prevalence of AD and rate of progression from MCI differe between males and females, it was critical that the analyses in the current study considered the possibility for sex differences in RSC dysfunction[31].

To address this overarching question, we investigated the RSC of 5xFAD mice to determine whether there were AD-related changes in neuronal activity. We first confirmed that the hypometabolic/hyperactive phenotype observed in the human RSC was also evident in the 5xFAD model. Indeed, we observed both increased excitability during memory retrieval, using c-Fos activity, and decreased metabolism based on reduced cytochrome C oxidase labeling. Intriguingly, these deficits were observed only in female but not male 5xFAD mice. To interrogate the increased excitability of the RSC, we performed whole cell patch clamp electrophysiology, we identified an increase in the excitability of pyramidal cells in the RSC of 5xFAD mice, particularly in females. Neuronal hyperexcitability is a commonly observed phenotype in AD mice. In addition, imaging studies in patients with MCI and AD suggests that there are regional and temporal changes in excitability. Patients with MCI have hyperactivity in some brain regions[32,33] while AD is associated with hypoactivity in the same regions suggesting a temporal progression with hyper- to hypo- excitability[34,35]. The underlying mechanisms of this transition are not completely understood. In our current study the sex-dependent hyperexcitability in the RSC pyramidal neurons coincided with an early impairment in activity of the PV-INs. The deficit in PV-IN activity could, lead to reduced inhibition of neurons within the RSC, and could ultimately explain the increased hyperexcitability of pyramidal neurons and the overall increased population activity in female 5xFAD mice[36,37]. The emergence of two distinct PV-IN populations in female 5xFAD mice (one normal and one impaired) may represent different stages of degeneration. Alternatively, PV-INs are a major subclass of cortical inhibitory interneurons but the make-up of this class is known to be heterogeneous[13,38] (e.g. basket versus chandelier cells). As such, the two populations may represent distinct subclasses of PV-INs that respond differentially during neurodegeneration.

As the most numerous class of interneurons in the cortex, PV-INs play a critical role in regulating neuronal excitability[12]. PV-INs synapse extensively onto pyramidal neurons as well as onto other inhibitory interneurons, including other PV-INs[39,40]. Individual PV-INs synapses onto multiple pyramidal cells each of which will also typically receive input from multiple PV-INs. We found here that the reduction in presynaptic PV-IN connectivity is significantly greater on CaMKII+ neurons than onto other PV-INs. It is not immediately clear why there is a differential loss of PV-IN synapses on different cell types. However, this finding does provide additional support for the increased excitability of RSC pyramidal neurons being due to a reduction in inhibition from PV-INs.

Along with the disrupted PV-IN activity, we also show here a significant reduction in the number of PV-INs in the RSC. Given that AD is a neurodegenerative disease, neuronal death is not inherently surprising[41]. However, there are several unique aspects related to the loss of PV-INs observed here. First, this deficit in PV-IN expression was, evident at a relatively early stage (6 months old) in female 5xFAD mice but was not present in age-matched males. However, in 12-month-old mice PV-IN loss was observed in both female and male 5XFAD mice, compared to controls. Importantly, the loss of PV-INs in 6-month-old female 5xFAD mice was selective to the RSC and not observed in other brain regions that show early AD pathology but they were lost by 12 months of age in other regions as well. The increased vulnerability of the PV-IN population in the RSC also stands out compared to the general neuron loss in this region which occurs at a much lower rate. All together these findings indicate that PV-INs in the female RSC are an attractive target for early intervention because they exhibit a unique, early vulnerability to AD.

The chemogenetic inhibition of PV-INs in healthy mice demonstrating the functional consequences of disrupted PV-IN activity also recapitulated the impairments that we observed in 5xFAD mice, including disruptions in the RSC functional connectivity, RSC regional excitability and behavior. The chemogenetic stimulation of PV-INs in the 5xFAD mice was able to rescue these impairments further supporting the integral role of RSC PV-INs in the establishment of AD-related disruptions. These findings provide a proof of principle for a targeted intervention strategy to promote cognitive enhancement. Even at an advanced age, which corresponds to a relatively progressive stage in AD, the targeting of RSC PV-INs activity was sufficient to enhance memory performance. This further strengthens the significance of improving the function of this specific cell type as a promising approach for effective treatment in AD. However, it is important to consider that the stimulation of the PV-IN population may be partially limited by the fact the disrupted PV activity in the RSC is accompanied by a reduction in the number (and connectivity) of PV-INs. Future studies should explore alternative approaches aimed at preventing the loss of PV-INs and preserving their connectivity. Such strategies, whether utilized independently or in conjunction with targeted PV-IN stimulation, have the potential to delay the onset of cognitive impairment, particularly in females, where such deficits manifest earlier and more profoundly[42–45].

An important overarching finding in the current study is the sex-specificity of the PV-IN dysfunction. Clinically, the incidence of AD is approximately two-fold greater and the rate of progression from MCI to AD is considerably more rapid in women than in men[29,30]. However, despite these well-established discrepancies, sex-stratified data from randomized clinical trials of AD treatments is scarce[46,47]. Even when considering pre-clinical models, the potential for sex differences is often not reported or assessed[48,49]. The results of the current study identify both a sex difference in the baseline expression density of PV-INs in female humans and mice. Furthermore, our results suggest an increased vulnerability of PV-INs to AD pathology at earlier stages of disease progression. Combined, these data add to the complex myriad of factors which contribute to sex-differences in the clinical prevalence and progression of AD, while also demonstrating the potential of PV-INs as a target of intervention.

Overall, our current study identifies a novel impairment in PV-IN function in the RSC, an understudied brain region with respect to AD. Importantly, these findings mirror the earlier cognitive impairments observed in females. As a result, our findings provide both a potential mechanism to explain why this sex difference occurs and, a specific intervention target to enhance cognition. Protection of the vulnerable PV-IN cell population may represent an important key to slowing cognitive decline in MCI/AD patients.

## Methods

### Subjects:

*Mice*:

Heterozygous 5xFAD mice were produced via *in vitro fertilization by the* University of Calgary Centre for Genome Engineering. Sperm was obtained from male 5xFAD mice (#034840-JAX) and female C57Bl/6J mice were used as oocyte donors(#000664-JAX). Male and female experimental offspring were aged to 6 or 12 months for use in most experiments. Experiments in which PV-IN activity was chemogenetically silenced were conducted using 8-week-old male and female C57Bl/6J mice. Further histological analyses were also conducted using male and female offspring from a TgCRND8 (MGI: 3589475) and C57Bl/6J cross, aged to 5 months. Mice were housed in standard cages with three to five mice per cage and free access to food and water. The room lighting was maintained on a 12 h/12 h light/dark cycle (8 am, lights on). All procedures were conducted during the light cycle phase. All experiments involving animal subjects were conducted in accordance with Canadian Council on Animal Care guidelines and with the approval of the University of Calgary Animal Care Committee.

*Human tissue samples*:

Frozen-fixed RSC tissue from male and female patients with Alzheimer's disease (Mean Age +/- SD: Male 71.2 +/- 3.3, Female 72.7 +/- 2.6) and age-matched individuals without Alzheimer's disease (Mean Age +/- SD: Male 69.3 +/- 2.8, Female 71.6 +/- 3.0) was obtained from the Douglas-Bell Canada Brain Bank (Montreal, QC, CA). The known average duration of disease was 8.1 +/- 3.4 years in Males AD patients and 7.4 +/- 4.6 years in female AD patients. In collaboration with the Quebec Coroner's Office and with informed consent from the next of kin, phenotypic information was obtained with standardized physiological autopsies. Control and Alzheimer's disease were defined with the support of medical charts and Coroner records. Toxicological assessments, medication prescription, and cognitive assessments were also obtained. All experiments involving human tissue samples were conducted with the approval of the University of Calgary Conjoint Health Research Ethics Board (REB22-0776).

### Electrophysiology:

400 μm coronal slices comprising the RSC were obtained in oxygenated ice-cold sucrose/ACSF using the Leica VT1000 S vibratome. Slices were recovered at 30C in ACSF (128 mM NaCl, 10 mM D-glucose, 26 mM $NaHCO_3$, 2 mM $CaCl_2$, 2 mM $MgSO_4$, 3 mM KCl, 1.25 mM $NaH_2PO_4$, pH7.4) saturated with 95% $O_2$ and 5% $CO_2$. Recordings were performed after a minimum 2-hour recovery. Patch pipettes (2-4 MOhm) contained the following internal patch solution: 120 mM

potassium gluconate, 10 mM HEPES, 5 mM KCl, 2 mM $MgCl_2$, 4 mM $K_2$-ATP, 0.4 mM $Na_2$-GTP, 10 mM $Na_2$-phosphocreatine, at pH 7.3. Neurons were visualized using the IR-DIC on an Olympus BX51WI microscope. Whole-cell patch clamp recordings were performed in current-clamp and voltage-clamp mode using a MultiClamp 700B amplifier (Molecular Devices). In current-clamp mode, action potentials were elicited by applying 500 ms depolarizing current pulses with a step size of 50 pA. For sIPSC recordings, patch pipettes contained the high $Cl^-$ patch solution: 50 mM K-gluconate, 10 mM HEPES, 75 mM KCl, 2 mM $MgCl_2$, 4 mM $K_2$-ATP, 0.4 mM $Na_2$-GTP, 10 mM $Na_2$-phosphocreatine, at pH 7.3. sIPSC recordings were performed in voltage clamp mode in the presence of 20 μM AMPA/Kainate receptor antagonist CNQX (Tocris) and 50 μM NMDA receptor antagonist AP5 (Tocris). Data were filtered at 4 kHz and digitized at 20 kHz using Digidata 1550B and Clampex software (Molecular Devices). Recordings were analyzed using pClamp 10.7 or Easy Electrophysiology.

**Behavioral testing:**

Mice were habituated to handling for 5 days prior to all behavioral tasks. In all tasks, mouse behavior was tracked using ANYmaze Behavioral Tracking Software (Stoelting Co., Wood Dale, IL, USA). Before and after each trial, all apparatuses and object cues were cleaned using 70% EtOH.

*Forced Alternation*:

Working memory ability was assessed using a Y-maze forced alternation task. The arms of the Y-maze apparatus were 41.5 cm long and 7.5 cm wide. Mice were placed at the end of one arm of the Y maze allowed 5 min to explore the apparatus. During this trial, one of the arms of the Y-maze was blocked. After a 30 min inter-trial interval, mice were returned to the Y-maze and were given 5 min to explore the apparatus without any of the arms being blocked. Time spent in the novel arm of this maze was assessed as a percentage of the total exploratory time, defined as the total time remaining in the task after the animal first leaves the start arm.

*Novel Object Location Task*:

Object location memory was assessed using a novel object location task. Mice were given a 5 min acclimation session with two identical objects in adjacent corners of a square 46.5 cm X 46.5 cm apparatus. Following the acclimation trial, mice were returned to a clean home cage while one of the identical objects was moved to the corner opposite of the other object. Mice were then given 5 min to explore the objects in the novel configuration. The time spent interacting with, defined as facing the object while in close proximity, the object in the novel location was expressed as a percentage of the total time spent interacting with either object.

*Contextual Conditioning Task*:

Contextual conditioning took place in Ugo Basile (Gemonio, Italy) contextual fear conditioning chambers (17 cm X 17 cm) placed inside of sound attenuating cabinets. During the 5 min conditioning trial, mice were allowed to explore the chamber for 2 min prior to the delivery of three shocks (1 mA, 2 s), each separated by an interval of 1 min. Mice were removed from the

conditioning chamber 1 min after the final shock and returned to the home cage. Context reintroduction took place 24 h later, during which mice were returned to the conditioned context for a 5 min trial without any shocks. Freezing was used as the primary measure of memory retention and was defined as a complete lack of motion, except for respiration, for at least one second. In cases of baseline differences in freezing during the initial conditioning trials, activity suppression was used to assess memory retention. Activity suppression was calculated as the distance travelled during the first 2 min of the retention trial divided by the total distance travelled during the first two minutes of the retention and conditioning trials[50].

**Histology:**

*Mouse tissue: perfusion and tissue processing*:

Ninety minutes following the completion of contextual conditioning tasks, mice were deeply anesthetized with isoflurane and transcardially perfused with 0.1 M phosphate-buffered saline (PBS) and 4% formaldehyde. Brains were extracted and postfixed in 4% formaldehyde at 4 °C for 24 h before cryoprotection in 30% w/v sucrose solution in PBS for two to three days until no longer buoyant. Brains were sectioned 50 μm thick on a cryostat (Leica CM 1950, Concord, ON, Canada) in 12 series. Sections were kept in a buffered antifreeze solution containing 30% ethylene glycol and 20% glycerol in 0.1 M PBS and stored at -20 °C.

*Immunofluorescent staining*:

For all immunofluorescent staining, tissue sections were washed three times (10 min per was) in 0.1 M PBS at room temperature. Sections were then incubated at room temperature in primary antibody solution, containing primary antibody, 3% normal goat serum, and 0.3% Triton X-100 (see Supplementary Table 1 for antibody information, dilutions, and incubation times). Following primary incubation, tissue was washed in 0.1 M PBS (3 x 10 mins) prior to incubation in secondary antibody solution (see Supplementary Table 1) in 0.1 M PBS at room temperature. Finally, tissues were counterstained with DAPI (20 mins, 1:1000 in 0.1 M PBS) before being washed in 0.1 M PBS (2 x 10 mins) and mounted to glass slides. Slides were coverslipped with PVA-DABCO mounting medium.

*Human tissue: tissue processing*:

Human tissue samples previously fixed and stored in formalin fixative, were cryoprotected in 30% w/v sucrose solution in 0.1 M PBS for 3 – 5 days. Tissue was sectioned 50 μm thick on a cryostat (Leica CM 1950, Concord, ON, Canada) in 12 series. Sections were stored at -20 °C in a buffered antifreeze solution containing 30% ethylene glycol and 20% glycerol in 0.1 M PBS.

*Peroxidase staining*:

Human tissue sections were stained as previously described[51]. Briefly, samples were rinsed in 0.1 M tris-buffered saline (TBS) for 10 min prior to a 10 min incubation in BLOXALL (Vector Laboratories, SP-6000) at room temperature. Tissue was then rinsed with TBS (2 X 5 min) before being incubated in a solution of 2.5% normal goat serum in TBS for 20 minutes. After the serum incubation, tissue was transferred to a primary antibody solution with a 1:500 concentration of anti-parvalbumin antibody (Invitrogen, PA1-933), 2.5% normal goat serum, and 0.3% Triton X-

100 in 0.1 M TBS at 4 °C. Tissue was then washed with 0.1 M TBS (5 X 5 min) and incubated in ImmPRESS HRP goat anti-rabbit IgG polymer detection kit reagent (Vector Laboratories, MP-74551) for 18 h at 4 °C. Following this incubation, tissue was washed with 0.1 M TBS (5 X 5) and the stain was allowed to develop for 2 minutes using an ImmPACT novaRED Substrate Kit (Vector Laboratories, SK-4805). Tissue sections were then washed for 5 min in tap water, followed by rinses in 0.1M TBS (2 x 5 min). Sections were mounted on glass slides and dried on a slide warmer for 15 minutes and were then dehydrated in two 3-minute incubations in isopropyl alcohol. Slides were coverslipped with VectaMount Express Mounting Medium (H-5700).

**Imaging and image analysis:**

*Optical density analyses*:

The optical density of cytochrome C oxidase and GLUT3 expression was assessed using images collected at 10X magnification (N.A. 0.4) using an OLYMPUS VS120-L100-W slide scanning microscope (Richmond Hill, ON, CA). Brightfield microscopy was used in collecting these images for the cytochrome C oxidase-stained tissue, while TRITC and DAPI filter cubes were used to collect images of the GLUT3-stained tissue. All optical density analyses were conducted using ImageJ.

*Cellular density analyses*:

The density of parvalbumin, NeuN, and c-Fos expression density in mouse brain tissue was assessed using images collected at 10X magnification (N.A. 0.4) using an OLYMPUS VS120-L100-W slide scanning microscope (Richmond Hill, ON, CA). In fluorescently stained mouse tissue, labels were segmented from background based on label size and fluorescent intensity using the user-guided machine learning image processing software *Ilastik*. Binary segmented labels were exported from *Ilastik* and their expression density was assessed within the RSC based on a tracing of this region in the accompanying DAPI channel image in ImageJ.

In human tissue PV-INs were segmented using the machine-learning based TrueAI software from OLYMPUS. With this segmentation, the machine learning protocol was trained to a subset of manually classified PV-INs and allowed one million iterations to establish a classification algorithm. The accuracy of this algorithm was assessed at 5,000, 10,000, 25,000, 100,000, 250,000, and 500,000 iterations. In mouse and human analyses, all cell counts were normalized based on the area of the RSC.

*Synaptotagmin-2 analyses*:

Analyses of Syt2 expression were conducted using an OLYMPUS FV3000 confocal microscope equipped with a 60X oil immersion objective (N.A. 1.42). In assessing the broad expression density of Syt2 in the RSC, volumetric scans (60X total magnification; 10 z steps; 0.35 μm z spacing) were collected in this region. Syt2 puncta were segmented from maximum intensity projections of these image stacks using *Ilastik* and their density was assessed using ImageJ. To assess the density of Syt2 puncta on PV-INs and CaMKII+ cells, a 5X zoom was applied for the collection of 20 volumetric scans (300x total magnification; full cells in z dimension; 0.35 μm z spacing) per mouse. Maximum intensity projections were generated from the top half of each volumetric scan and Syt2 puncta were segmented using *Ilastik*. PV+ and CaMKII+ cells were

traced using ImageJ and the density of Syt2 puncta was assessed within the bounds of these tracings.

*Functional connectivity analyses*:
Brain-wide c-Fos expression was imaged using an OLMYPUS VA120-L100-W slide scanning microscope (Richmond Hill, ON, CA) equipped with a 10X objective (N.A. 0.4). Using *Ilastik*, c-Fos+ cells were segmented to generate binary masks of brain-wide c-Fos expression[52]. These binary masks were then registered to the Allen Mouse Brain Reference Atlas using a modified protocol building upon *Whole Brain*[53,54]. Using custom MATLAB analyses, outputs were organized to yield c-Fos expression densities across 90 neuroanatomical regions (for a detailed list of regions, see Supplementary Table 2). Regional c-Fos expression density was correlated across groups for all possible combinations of regions, generating correlation matrices of regional co-activation for each group[55]. From each co-activation matrix, the functional connectivity of the RSC was assessed using calculation derived from the Brain Connectivity Toolbox[56]. For analyses of binary network characteristics, such as local efficiency and clustering coefficient, co-activation matrices were binarized to adjacency matrices using thresholding criteria of $P < 0.05$ and Pearson's $R > 0.8$.

*Validation of viral targeting*:
Prior to any statistical analyses in the fiber photometry and chemogenetic experiments, the accuracy of virus/optic fiber targeting. For this validation, a series of DAPI-stained tissue sections from each mouse were scanned at 10X magnification (N.A. 0.4) using an OLYMPUS BX-63 epifluorescent microscope (Richmond Hill, ON, CA). The location and spread of the viral injections were then assessed, blind to treatment, relative to the target surgical coordinates using the Allen Mouse Brain Reference Atlas as a reference. All data from any mice showing inadequate viral targeting or expression was excluded from analyses.

Fiber photometry experiment:
*Surgical procedures*:
Surgeries were conducted under isoflurane delivered via a Somnosuite anaesthetic delivery system (Kent Scientific) drawing pure compressed oxygen. Mice were induced at 5% isoflurane before being transferred to a stereotaxic head frame (Kopf) and maintained at 1-2% isoflurane. Analgesia (Metacam, 5 mg/kg) and fluid support (warmed saline, 0.5 mL) were given at the beginning of the surgery. The scalp was shaved and cleaned with alternating chlorhexidine and 70% ethanol scrubs prior to midline incision, exposing the skull. A robotic stereotaxic manipulator paired with stereodrive software (Neurostar) was used to drill burr holes prior to virus injection via a glass infusion needle attached to a Nanoject III infusion system (Drummond Scientific). Virus (AAV1-S5E2-jGCaMP6f; Addgene #135632-AAV1; diluted 1:3 in saline) was injected into the RSC (AP: -3.1; ML: -0.5; DV: 1.1) in six sets of 50 nL pulses at a rate of 10 nL/s with 10 s between pulses. The pipette was left at the target depth for 5 minutes following the final pulse to allow for diffusion of the virus before being raised slowly. Following virus injection, a fiber optic implant (N.A. 0.37, core 200 μm, 2.0 mm length) was lowered into the RSC at the injection site (AP: -3.1; ML: -0.5; DV: 1.0). Implants were secured to the skull by applying a thin

layer of superglue to the exposed surface of the skull around the base on the implant. This layer was then covered with black, opaque, dental acrylic to form a headcap. Once the headcap was set, the incision was closed with suture material and mice were removed from the stereotaxic frame. Mice were allowed to recover for 2 weeks while receiving additional Metacam doses for 3 days after surgery.

*Photometry recordings*:
Mice were habituated to being connected to the fiber optic path cord (Doric) for 3 consecutive days. Photometry recordings were collected using a FP3002 Neurophotometrics system controlled by Bonsai software. Prior to the start of each behavioral test, a 5-minute baseline photometry recording was taken in a clean and empty home cage. Recordings occurred throughout the entire duration of the behavioral task and behavior was time locked to the photometry signal through a TTL pulse generated by ANYmaze tracking software (Stoelting) which was integrated into the Neurophotometrics photometry data. Recordings were acquired at 40 FPS, with 470 nm and 415 nm channels being active in alternating frames, resulting in an effective framerate of 20 FPS for each channel. Both the 470 nm channel and the 415 nm isosbestic channel were calibrated to 50 uW using a photometer (Thor Labs PM100D).

*Photometry analysis*:
Photometry recordings were analyzed using custom MATLAB scripts[57]. Behavioral information recorded using ANYmaze was integrated into the analysis using a nearest neighbour approach, by indexing through the photometry data and aligning behavioral data based on the minimum difference between pairs of timestamps. Data from the isosbestic 415 nm channel was fit to a biexponential decay to correct for photobleaching. The resulting vector was used to linearly scale calcium-dependent data collected using the 470 nm channel. To calculate $\Delta F$, these linearly scaled calcium-dependent data were subtracted from the raw unprocessed calcium-dependent data. The resulting values were then divided by the linearly scaled calcium-dependent data to generate a $\Delta F/F$ trace.

**Chemogenetic experiments:**
*Viruses*:
All virus was diluted 1:3 in sterile saline prior to injection. For chemogenetic inhibition experiments, mice received injections of either hM4Di virus or a control virus (pAAV-S5E2-GFP; Addgene #135631-AAV1). The hM4Di virus was derived from Addgene plasmid 83896. The hDlx enhancer element was removed and replaced with the S5E2 regulatory element and packaged as AAV1 by the Hotchkiss Brain Institute Molecular Core Facility. For the experiments with chemogenetic activation, all mice received injections of a hM3Dq virus (pAAV-S5E2-Gq-P2A-dTomato; Addgene #135635-AAV1)[58].

*Surgical procedures*:
Surgical procedures were conducted as described in the fiber photometry experiments. Virus was injected in four 50 nL pulses at a rate of 10 nL/s with 10 s between pulses at the anterior (AP: -0.9; ML: +/-0.3; DV: 1.2) and posterior (AP: -2.2; ML: +/-0.3; DV: 1.0) portions of the RSC. The pipette

was left in the target for 5 minutes following the final pulse before being slowly raised out of the brain. The incision was then closed with suture material and mice were removed from the stereotaxic frame. Mice were allowed to recover for 2 weeks while receiving additional Metacam doses for 3 days after surgery.

*DCZ preparation and administration*:
Deschloroclozapine dihydrochloride (DCZ; HelloBio HB126-25mg) was diluted in saline for a working dose of 3 μg/kg (0.3 mg/mL, inj. at 0.01 mL/g)[59]. For chemogenetic inhibition experiments, all mice received DCZ treatment 15 minutes prior to the start of each behavioral test. For chemogenetic activation experiments, mice received either DCZ treatment or saline injection (0.01 mL/g) 15 minutes prior to the start of each behavioral test.

Statistics and data visualization
All statistical analyses were performed in Prism (GraphPad Software, Version 9.4.0) or with standard MATLAB functions and statistical tests. Independent t-tests; three-, two-, and one-way ANOVAs; and Pearson's Correlations were performed. Data in graphs is presented as mean ± s.e.m. Hypothesis testing was complemented by estimation statistics for each comparison using estimationstats.com. For these estimation statistics, the effect size (Cohen's d) was calculated using a bootstrap sampling distribution with 5000 resamples along with a 95% confidence interval (CI; bias-corrected and accelerated). Data distribution was assumed to be normal, but this was not formally tested. Statistical methods were not used to predetermine study sizes but were based on similar experiments previously published. Experimenters were blinded to the genotype and sex of the animals during all analyses. Experimenters were blinded to all identifying features when analyzing human tissue samples. All statistical comparisons and outputs are included in Supplementary Tables 3 and 4. All plots were generated in Prism or MATLAB. Circle plots were generated using the circularGraph MATLAB function. Some of the schematics were generated using images from BioRender. All figures were compiled in Adobe Photoshop.

**Data availability:**
The data that support the findings of this study are available in the manuscript or the supplementary materials and have been made publicly available at the following GitHub repository: https://github.com/dterstege/PublicationRepo/tree/main/Terstege2023A.

**Code availability:**
All analysis code used to generate the results reported in the manuscript, instructions on how to use these analyses, and sample datasets have been made publicly available at the following GitHub repository: https://github.com/dterstege/PublicationRepo/tree/main/Terstege2023A.

References

1. Minoshima, S. *et al.* Metabolic reduction in the posterior cingulate cortex in very early Alzheimer's disease. *Ann. Neurol.* **42**, 85–94 (1997).
2. Greicius, M. D., Srivastava, G., Reiss, A. L. & Menon, V. Default-mode network activity distinguishes Alzheimer's disease from healthy aging: evidence from functional MRI. *Proc. Natl. Acad. Sci. U. S. A.* **101**, 4637–4642 (2004).
3. Strom, A. *et al.* Cortical hypometabolism reflects local atrophy and tau pathology in symptomatic Alzheimer's disease. *Brain* **145**, 713–728 (2022).
4. Nestor, P. J., Fryer, T. D., Ikeda, M. & Hodges, J. R. Retrosplenial cortex (BA 29/30) hypometabolism in mild cognitive impairment (prodromal Alzheimer's disease). *Eur. J. Neurosci.* **18**, 2663–2667 (2003).
5. Ash, J. A. *et al.* Functional connectivity with the retrosplenial cortex predicts cognitive aging in rats. *Proc. Natl. Acad. Sci. U. S. A.* **113**, 12286–12291 (2016).
6. Kaboodvand, N., Bäckman, L., Nyberg, L. & Salami, A. The retrosplenial cortex: A memory gateway between the cortical default mode network and the medial temporal lobe. *Hum. Brain Mapp.* **39**, 2020–2034 (2018).
7. Rolls, E. T., Wirth, S., Deco, G., Huang, C.-C. & Feng, J. The human posterior cingulate, retrosplenial, and medial parietal cortex effective connectome, and implications for memory and navigation. *Hum. Brain Mapp.* **44**, 629–655 (2023).
8. Oakley, H. *et al.* Intraneuronal beta-amyloid aggregates, neurodegeneration, and neuron loss in transgenic mice with five familial Alzheimer's disease mutations: potential factors in amyloid plaque formation. *J. Neurosci.* **26**, 10129–10140 (2006).
9. Hämäläinen, A. *et al.* Increased fMRI responses during encoding in mild cognitive impairment. *Neurobiol. Aging* **28**, 1889–1903 (2007).
10. Sperling, R. A. *et al.* fMRI studies of associative encoding in young and elderly controls and mild Alzheimer's disease. *J. Neurol. Neurosurg. Psychiatry* **74**, 44–50 (2003).
11. Tamamaki, N. *et al.* Green fluorescent protein expression and colocalization with calretinin, parvalbumin, and somatostatin in the GAD67-GFP knock-in mouse. *J. Comp. Neurol.* **467**, 60–79 (2003).
12. Rudy, B., Fishell, G., Lee, S. & Hjerling-Leffler, J. Three groups of interneurons account for nearly 100% of neocortical GABAergic neurons. *Dev. Neurobiol.* **71**, 45–61 (2011).
13. DeFelipe, J. Neocortical neuronal diversity: chemical heterogeneity revealed by colocalization studies of classic neurotransmitters, neuropeptides, calcium-binding proteins, and cell surface molecules. *Cereb. Cortex* **3**, 273–289 (1993).
14. Azhar Chishti, M. *et al.* Early-onset Amyloid Deposition and Cognitive Deficits in Transgenic Mice Expressing a Double Mutant Form of Amyloid Precursor Protein 695 *. *J. Biol. Chem.* **276**, 21562–21570 (2001).
15. Ali, F., Baringer, S. L., Neal, A., Choi, E. Y. & Kwan, A. C. Parvalbumin-positive neuron loss and amyloid-β deposits in the frontal cortex of Alzheimer's disease-related mice. *J. Alzheimers. Dis.* **72**, 1323–1339 (2019).

16. Solodkin, A., Veldhuizen, S. D. & Van Hoesen, G. W. Contingent vulnerability of entorhinal parvalbumin-containing neurons in Alzheimer's disease. *J. Neurosci.* **16**, 3311–3321 (1996).
17. Poon, C. H. *et al.* Sex differences between neuronal loss and the early onset of amyloid deposits and behavioral consequences in 5xFAD transgenic mouse as a model for Alzheimer's Disease. *Cells* **12**, 780 (2023).
18. Waller, R., Mandeya, M., Viney, E., Simpson, J. E. & Wharton, S. B. Histological characterization of interneurons in Alzheimer's disease reveals a loss of somatostatin interneurons in the temporal cortex. *Neuropathology* **40**, 336–346 (2020).
19. Schwab, C., Yu, S., Wong, W., McGeer, E. G. & McGeer, P. L. GAD65, GAD67, and GABAT immunostaining in human brain and apparent GAD65 loss in Alzheimer's disease. *J. Alzheimers. Dis.* **33**, 1073–1088 (2013).
20. Keene, C. S. & Bucci, D. J. Damage to the retrosplenial cortex produces specific impairments in spatial working memory. *Neurobiol. Learn. Mem.* **91**, 408–414 (2009).
21. Fournier, D. I., Eddy, M. C., DeAngeli, N. E., Huszár, R. & Bucci, D. J. Retrosplenial cortex damage produces retrograde and anterograde context amnesia using strong fear conditioning procedures. *Behav. Brain Res.* **369**, 111920 (2019).
22. Hindley, E. L., Nelson, A. J. D., Aggleton, J. P. & Vann, S. D. Dysgranular retrosplenial cortex lesions in rats disrupt cross-modal object recognition. *Learn. Mem.* **21**, 171–179 (2014).
23. Stanley, M. L. *et al.* Changes in brain network efficiency and working memory performance in aging. *PLoS One* **10**, e0123950 (2015).
24. Mizuseki, K. & Buzsaki, G. Theta oscillations decrease spike synchrony in the hippocampus and entorhinal cortex. *Philos. Trans. R. Soc. Lond. B Biol. Sci.* **369**, 20120530 (2014).
25. Moretti, J., Terstege, D. J., Poh, E. Z., Epp, J. R. & Rodger, J. Low intensity repetitive transcranial magnetic stimulation modulates brain-wide functional connectivity to promote anti-correlated c-Fos expression. *Sci. Rep.* **12**, 20571 (2022).
26. Small, G. W. *et al.* Cerebral metabolic and cognitive decline in persons at genetic risk for Alzheimer's disease. *Proc. Natl. Acad. Sci. U. S. A.* **97**, 6037–6042 (2000).
27. Andersen, K. *et al.* Gender differences in the incidence of AD and vascular dementia: The EURODEM Studies. *Neurology* **53**, 1992–1992 (1999).
28. Gao, S., Hendrie, H. C., Hall, K. S. & Hui, S. The relationships between age, sex, and the incidence of dementia and Alzheimer disease: a meta-analysis. *Arch. Gen. Psychiatry* **55**, 809–815 (1998).
29. Buckley, R. F. *et al.* Sex mediates relationships between regional tau pathology and cognitive decline. *Ann. Neurol.* **88**, 921–932 (2020).
30. Levine, D. A. *et al.* Sex differences in cognitive decline among US adults. *JAMA Netw. Open* **4**, e210169 (2021).
31. Waters, A., Society for Women's Health Research Alzheimer's Disease Network & Laitner, M. H. Biological sex differences in Alzheimer's preclinical research: A call to action. *Alzheimers Dement. (N. Y.)* **7**, e12111 (2021).

32. Bassett, S. S. *et al.* Familial risk for Alzheimer's disease alters fMRI activation patterns. *Brain* **129**, 1229–1239 (2006).
33. Bookheimer, S. Y. *et al.* Patterns of brain activation in people at risk for Alzheimer's disease. *N. Engl. J. Med.* **343**, 450–456 (2000).
34. Celone, K. A. *et al.* Alterations in memory networks in mild cognitive impairment and Alzheimer's disease: an independent component analysis. *J. Neurosci.* **26**, 10222–10231 (2006).
35. Dickerson, B. C. *et al.* Increased hippocampal activation in mild cognitive impairment compared to normal aging and AD. *Neurology* **65**, 404–411 (2005).
36. Lu, J.-T., Li, C.-Y., Zhao, J.-P., Poo, M.-M. & Zhang, X.-H. Spike-timing-dependent plasticity of neocortical excitatory synapses on inhibitory interneurons depends on target cell type. *J. Neurosci.* **27**, 9711–9720 (2007).
37. Cardin, J. A. *et al.* Driving fast-spiking cells induces gamma rhythm and controls sensory responses. *Nature* **459**, 663–667 (2009).
38. Miyamae, T., Chen, K., Lewis, D. A. & Gonzalez-Burgos, G. Distinct physiological maturation of Parvalbumin-positive neuron subtypes in mouse prefrontal cortex. *J. Neurosci.* **37**, 4883–4902 (2017).
39. Fernandez, F. R., Via, G., Canavier, C. C. & White, J. A. Kinetics and connectivity properties of parvalbumin- and somatostatin-positive inhibition in layer 2/3 medial entorhinal cortex. *eNeuro* **9**, ENEURO.0441-21.2022 (2022).
40. Bartholome, O., de la Brassinne Bonardeaux, O., Neirinckx, V. & Rogister, B. A composite sketch of fast-spiking parvalbumin-positive neurons. *Cereb. Cortex Commun.* **1**, tgaa026 (2020).
41. Eimer, W. A. & Vassar, R. Neuron loss in the 5XFAD mouse model of Alzheimer's disease correlates with intraneuronal Aβ42 accumulation and Caspase-3 activation. *Mol. Neurodegener.* **8**, 2 (2013).
42. Hijazi, S. *et al.* Early restoration of parvalbumin interneuron activity prevents memory loss and network hyperexcitability in a mouse model of Alzheimer's disease. *Mol. Psychiatry* **25**, 3380–3398 (2020).
43. McDermott, B. *et al.* Gamma band neural stimulation in humans and the promise of a new modality to prevent and treat Alzheimer's disease. *J. Alzheimers. Dis.* **65**, 363–392 (2018).
44. Etter, G. *et al.* Optogenetic gamma stimulation rescues memory impairments in an Alzheimer's disease mouse model. *Nat. Commun.* **10**, (2019).
45. Verret, L. *et al.* Inhibitory interneuron deficit links altered network activity and cognitive dysfunction in Alzheimer model. *Cell* **149**, 708–721 (2012).
46. Canevelli, M. *et al.* Sex and gender differences in the treatment of Alzheimer's disease: A systematic review of randomized controlled trials. *Pharmacol. Res.* **115**, 218–223 (2017).
47. Martinkova, J. *et al.* Proportion of women and reporting of Outcomes by sex in clinical trials for Alzheimer disease: A systematic review and meta-analysis. *JAMA Netw. Open* **4**, e2124124 (2021).
48. Flórez-Vargas, O. *et al.* Bias in the reporting of sex and age in biomedical research on mouse models. *Elife* **5**, (2016).

49. Stranges, T. N., Namchuk, A. B., Splinter, T. F. L., Moore, K. N. & Galea, L. A. M. Are we moving the dial? Canadian health research funding trends for women's health, 2S/LGBTQ + health, sex, or gender considerations. *Biol. Sex Differ.* **14**, (2023).
50. Anagnostaras, S. G., Josselyn, S. A., Frankland, P. W. & Silva, A. J. Computer-assisted behavioral assessment of Pavlovian fear conditioning in mice. *Learn. Mem.* **7**, 58–72 (2000).
51. Epp, J. R., Beasley, C. L. & Galea, L. A. Increased hippocampal neurogenesis and p21 expression in depression: dependent on antidepressants, sex, age, and antipsychotic exposure. *Neuropsychopharmacology* **38**, 2297–2306 (2013).
52. Berg, S. *et al.* ilastik: interactive machine learning for (bio)image analysis. *Nat. Methods* **16**, 1226–1232 (2019).
53. Fürth, D. *et al.* An interactive framework for whole-brain maps at cellular resolution. *Nat. Neurosci.* **21**, 139–149 (2018).
54. Terstege, D. J., Durante, I. M. & Epp, J. R. Brain-wide neuronal activation and functional connectivity are modulated by prior exposure to repetitive learning episodes. *Front. Behav. Neurosci.* **16**, (2022).
55. Terstege, D. J. & Epp, J. R. Network neuroscience untethered: Brain-wide immediate early gene expression for the analysis of functional connectivity in freely behaving animals. *Biology (Basel)* **12**, 34 (2022).
56. Rubinov, M. & Sporns, O. Complex network measures of brain connectivity: uses and interpretations. *Neuroimage* **52**, 1059–1069 (2010).
57. Evans, A., Terstege, D. J., Scott, G. A., Tsutsui, M. & Epp, J. R. Neurogenesis mediated plasticity is associated with reduced neuronal activity in CA1 during context fear memory retrieval. *Sci. Rep.* **12**, 7016 (2022).
58. Vormstein-Schneider, D. *et al.* Viral manipulation of functionally distinct interneurons in mice, non-human primates and humans. *Nat. Neurosci.* **23**, 1629–1636 (2020).
59. Nagai, Y. *et al.* Deschloroclozapine, a potent and selective chemogenetic actuator enables rapid neuronal and behavioral modulations in mice and monkeys. *Nat. Neurosci.* **23**, 1157–1167 (2020).

**Acknowledgments:**
Funding for this study was provided by an Alzheimer's Society Research Program (ASRP) New investigator Grant (#21-05), a Canadian Foundation for Innovation (CFI) Grant (#38160), and a Women's Brain Health Initiative Grant in partnership with Brain Canada (#5542) to J.R.E. as well as an Alzheimer's Association Grant in partnership with Brain Canada (AARG-22-917644) to D.S. D.J.T. received a doctoral fellowship from NSERC (PGS D). Y.R. received a graduate fellowship from the Hotchkiss Brain Institute. The znp-1 monoclonal antibody (AB_2315626) developed by Bill Trevarrow and colleagues was obtained from the Developmental Studies Hybridoma Bank, created by the NICHD of the NIH and maintained by the University of Iowa, Department of Biological Sciences, Iowa City, IA, USA. AAV1-S5E2-jGCaMP6f (Addgene viral prep # 135632-AAV9 ; http://n2t.net/addgene:135632 ; RRID:Addgene_135632), pAAV-S5E2-GFP (Addgene viral prep # 135631-AAV1 ; http://n2t.net/addgene:135631 ; RRID:Addgene_135631), and pAAV-S5E2-Gq-P2A-dTomato (Addgene viral prep # 135635-AAV9 ; http://n2t.net/addgene:135635 ; RRID:Addgene_135635) were gifts from Jordane Dimidschstein. AAV-hDlx-GiDREADD-dTomato-Fishell-5 was a gift from Gordon Fishell (Addgene plasmid # 83896 ; http://n2t.net/addgene:83896 ; RRID:Addgene_83896). We acknowledge the Hotchkiss Brain Institute Advanced Microscopy Platform and the Cumming School of Medicine for support and use of the Olympus VS120-L100-W slide scanning microscope. We acknowledge Dr. Frank Visser and the Hotchkiss Brain Institute Molecular and Cellular Biology Core Facility for generating the S5E2-Gi-P2A-dTomato viral prep.

**Author Information:**

Authors and Affiliations
Department of Cell Biology and Anatomy, Cumming School of Medicine, University of Calgary, Calgary, AB, Canada
Dylan J. Terstege, Yi Ren, Jonathan R. Epp

Hotchkiss Brain Institute, University of Calgary, Calgary, AB, Canada
Dylan J. Terstege, Yi Ren, Derya Sargin, Jonathan R. Epp

Department of Psychology, University of Calgary, Calgary, AB, Canada
Derya Sargin

Alberta Children's Hospital Research Institute, University of Calgary, Calgary, AB, Canada
Derya Sargin

Contributions
D.J.T., D.S. and J.R.E. conceived the study and designed experiments. D.J.T. and Y.R. conducted the surgical procedures and behavioral experiments. D.S. conducted the electrophysiology experiments. D.J.T., Y.R., and J.R.E. conducted the histological experiments. D.J.T. wrote all code for all photometry and histological analyses. D.J.T. and J.R.E. conducted the data and statistical analyses. D.S. and J.R.E. secured funding for the experiments. D.J.T., D.S., and J.R.E. wrote the paper. All authors provided input and approved of the manuscript prior to submission.

Corresponding author
Correspondence to Jonathan R. Epp.

**Ethics declarations:**

Competing interests
The authors declare no competing interests.

## Figures

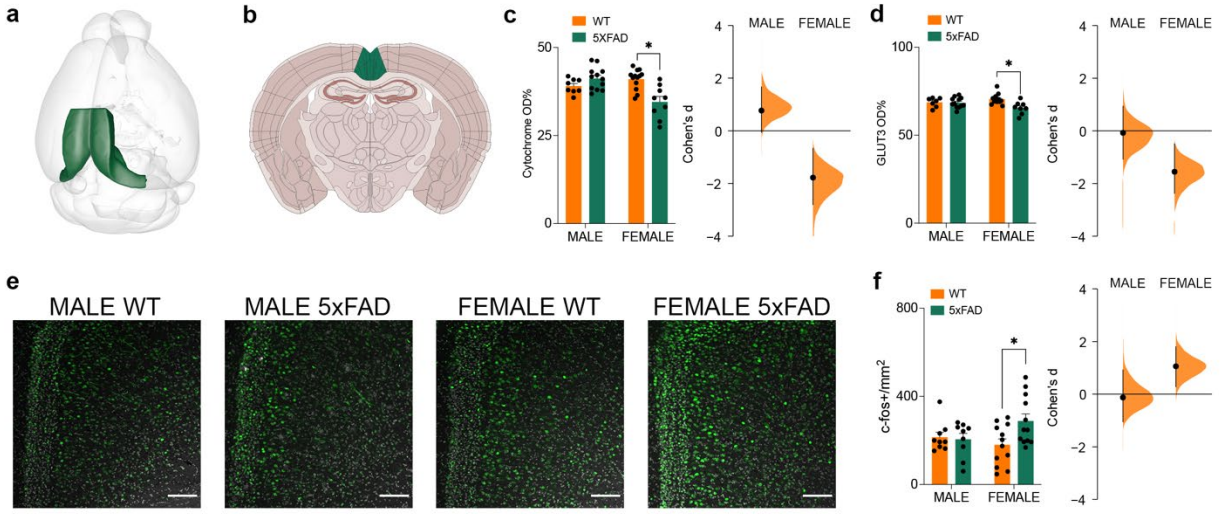


**Fig. 1: Hypometabolism and hyperexcitability of the RSC in female 5xFAD mice.**
**a**, Schematic highlighting the retrosplenial cortex in a 3D model of the adult mouse brain. **b**, Schematic illustrating the location of the retrosplenial cortex within a coronal plane of the Allen Mouse Brain Reference Atlas. **c**, The optical density of cytochrome C oxidase staining was decreased in the RSC of female 5xFAD mice (two-way ANOVA, sex X genotype interaction, $F_{(38)} = 17.55$, $P = 0.0002$; Tukey's multiple comparison test, Female WT vs. Female 5xFAD, $P = 0.0003$), indicating reduced mitochondrial activity. Effect size difference in the cytochrome C oxidase optical density across WT and 5xFAD groups for male (Cohen's D = 0.768) and female (Cohen's D = -1.75) mice. **d**, Optical density of GLUT3 staining in the RSC. The optical density of GLUT3 staining was decreased in the RSC of female 5xFAD mice (two-way ANOVA, sex X genotype interaction, $F_{(35)} = 5.606$, $P = 0.0298$; Tukey's multiple comparison test, Female WT vs. Female 5xFAD, $P = 0.0055$). Effect size difference in the optical density of GLUT3 across WT and 5xFAD groups for male (Cohen's D = -0.0773) and female (Cohen's D = -1.55) mice. **e**, Representative photomicrographs of c-Fos (green) and DAPI (greyscale) staining in the RSC of male and female WT and 5xFAD mice. **f**, The expression density of c-Fos+ cells was increased in female 5xFAD mice (two-way ANOVA, sex X genotype interaction, $F_{(38)} = 17.55$, $P = 0.0463$; Tukey's multiple comparison test, Female WT vs. Female 5xFAD, $P = 0.0367$), indicating hyperactivity. Effect size difference in c-Fos expression density across WT and 5xFAD groups for male (Cohen's D = -0.126) and female (Cohen's D = 1.06) mice. Scale bars represent 50 µm. Data represent mean ± SEM. $^*P < 0.05$. All statistical comparisons have been provided as a Stats Table file.

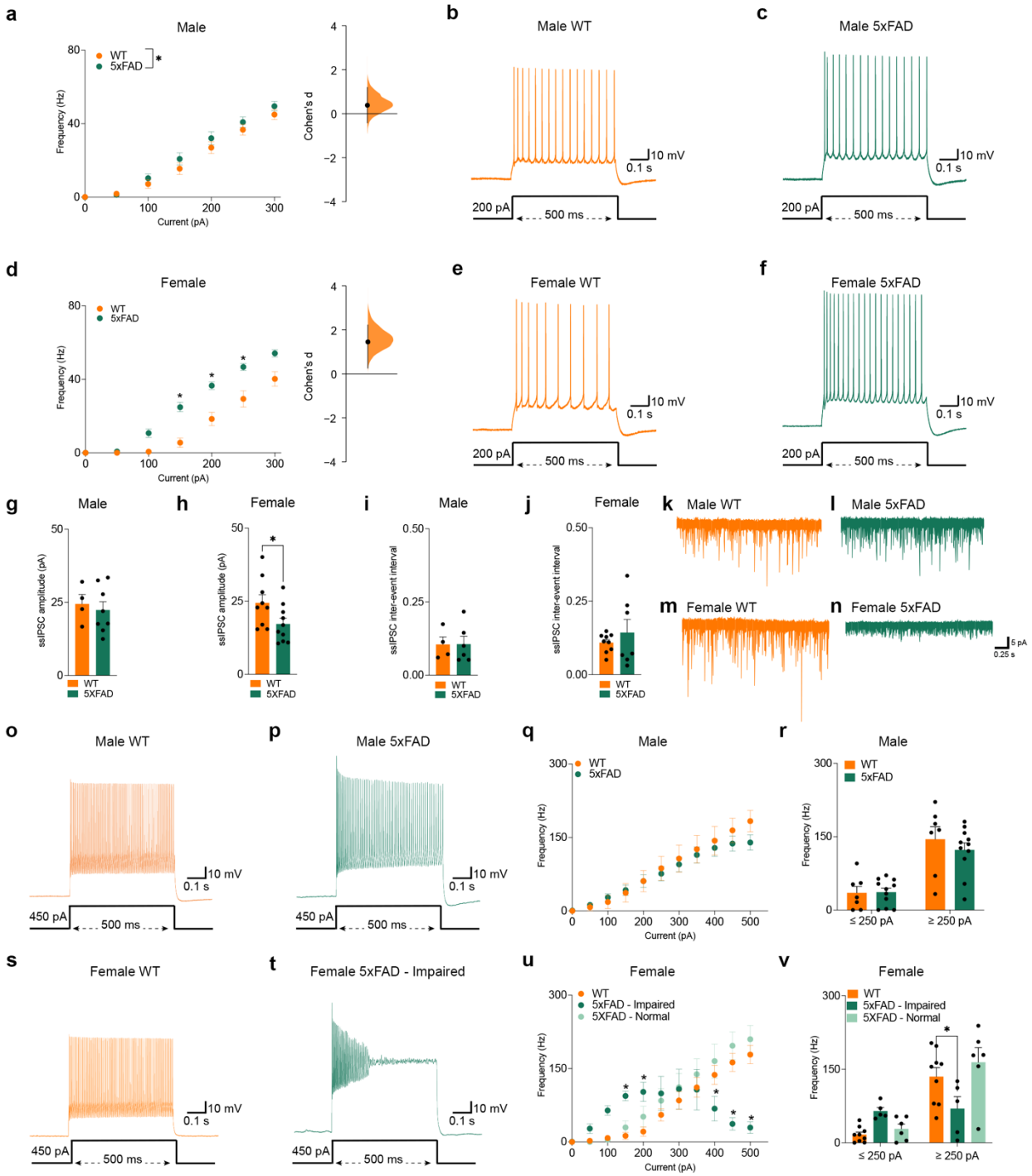


**Fig. 2: Hyperexcitable pyramidal neurons and impaired PV-IN activity in the RSC of female 5xFAD mice.**

**a**, Input-output curve showing spike frequency (Hz) of pyramidal cells in male mice in response to a series of depolarizing current (pA) injections. The firing frequency (Hz) of pyramidal cells in male 5xFAD mice (n = 12 cells) is elevated relative to male WT mice (n = 17 cells) indicating increased excitability (two-way repeated-measures ANOVA, effect of genotype, $F_{(189)} = 4.945$, $P =$

0.0273). Effect size difference in the summed firing frequency (Hz) across all depolarization steps between groups (Cohen's D = 0.282). Current-clamp traces of representative pyramidal cells from a male (**b**) WT and (**c**) a 5xFAD mouse in response to 200 pA current input. **d**, Input-output curve showing spike frequency (Hz) of pyramidal cells in female mice in response to a series of depolarizing current (pA) injections. The firing frequency (Hz) of pyramidal cells in female 5xFAD mice (n = 14 cells) is elevated relative to female WT mice (n = 9 cells) indicating increased excitability (two-way repeated-measures ANOVA, effect of genotype, $F_{(231)} = 66.63$, $P < 0.0001$). Effect size difference in the summed firing frequency (Hz) across all depolarization steps between groups (Cohen's D = 1.45). Current-clamp traces of representative PV-INs from a female (**e**) WT and (**f**) a 5xFAD mouse in response to 200 pA current input. **g**, sIPSC amplitude (pA) in male WT and 5xFAD mice. **h**, RSC pyramidal cells from female 5xFAD mice showed reduced sIPSC amplitude (two-sample t test, $t_{(17)} = 2.124$), compared with that of WT mice. **i**, sIPSCs inter-event interval (s) in male WT and 5xFAD mice. **j**, sIPSCs inter-event interval (s) in female WT and 5xFAD mice. Example sIPSC traces for (**k**) male WT, (**l**) male 5xFAD, (**m**) female WT, and (**n**) female 5xFAD mice. Representative current-clamp traces from PV-INs in (**o**) male WT, (**p**) male 5xFAD, (**s**) female WT, and (**t**) female 5xFAD – Impaired groups in response to a 450 pA depolarizing current input. **q**, Input-output curve showing spike frequency (Hz) of PV-INs in male mice in response to depolarizing current (pA) injections. **r**, The mean firing frequency (Hz) of PV-INs in male mice in response to ≤250 pA and ≥250 pA current input. **u**, Input-output curve showing spike frequency (Hz) of PV-INs in female mice in response to depolarizing current (pA) injections. Dichotomous responses from two different PV-IN populations in 5xFAD females are visible ("5xFAD – Impaired" vs "5xFAD – Normal"). **v**, The firing frequencies of the PV-IN populations in female 5xFAD mice differed from female WT mice (two-way, repeated measures ANOVA, current step X genotype interaction, $F_{(20, 187)} = 5.299$, $P < 0.0001$). Multiple comparisons revealed initial hyperexcitability in "5xFAD - Impaired" populations followed by subsequent impaired firing response in these cells. **v**, The mean firing frequency (Hz) of PV-INs in female mice in response to ≤250 pA and ≥250 pA current input. Firing rate was disrupted in 5xFAD – impaired PV-IN populations at high amplitude current injections (two-way repeated-measures ANOVA, Genotype X Current Step interaction, $F_{(2, 34)} = 6.937$, $P = 0.0030$; Dunnett's multiple comparison test, ≥ 250 pA WT s vs. ≥ 250 pA 5xFAD – Impaired, $P = 0.0252$), compared with WT PV-INs. Data represent mean ± SEM. *$P < 0.05$. All statistical comparisons have been provided as a Stats Table file.

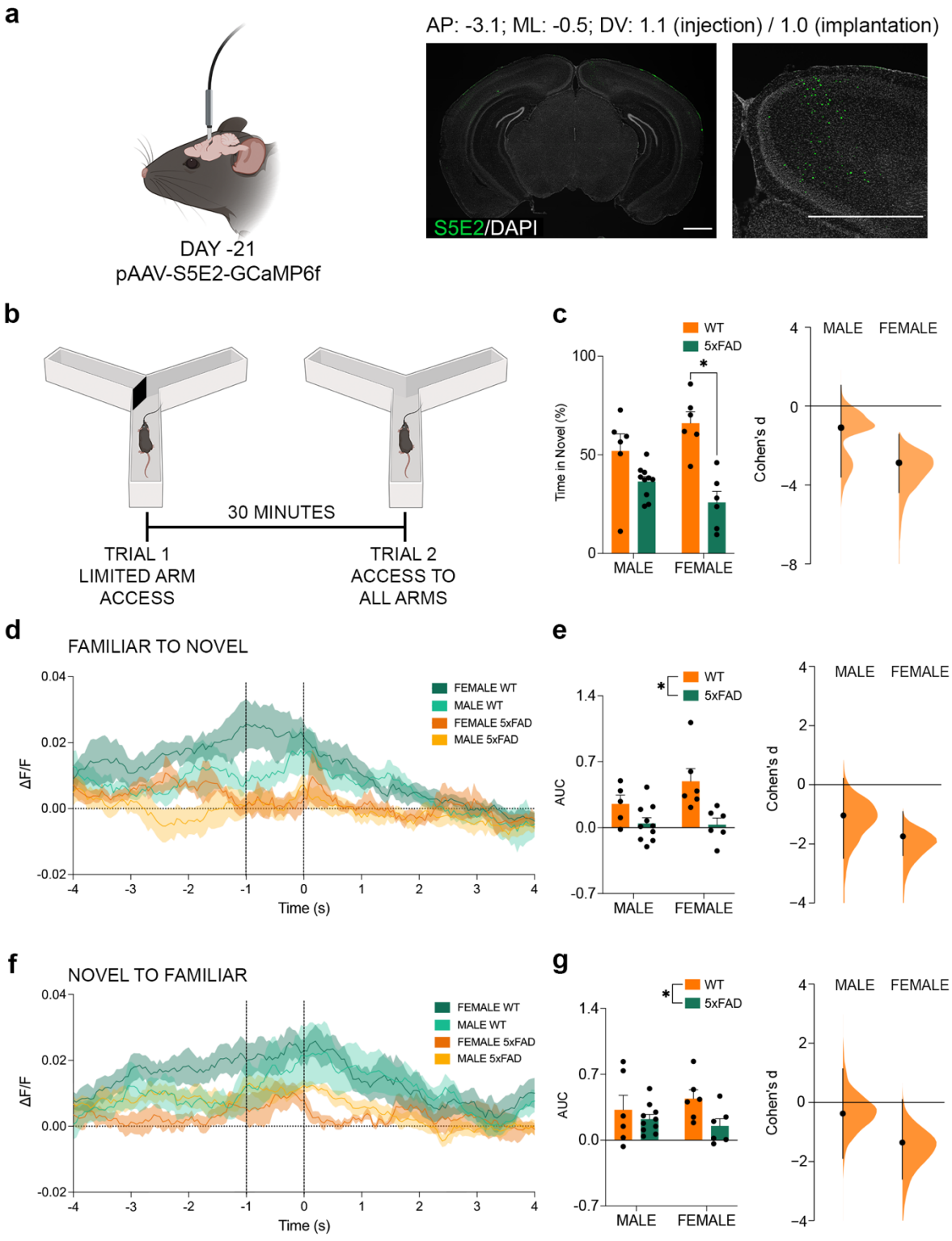


**Fig. 3: Impaired population activity of RSC PV-INs *in vivo* during working memory performance.**

**a**, Schematic showing pAAV-S5E2-GCaMP6f injection site, fibre optic ferrule placement, and virus expression. **b**, Design of the forced alternation y maze task. **c**, Percentage of time spent in

the novel arm of the y maze. Female 5xFAD mice spent less time, by percentage, in the novel arm of the maze than female WT mice (two-way ANOVA, Sex X Genotype interaction, $F_{(24)} = 5.034$, $P = 0.034$; Tukey's multiple comparison test, Female WT vs. Female 5xFAD, $P = 0.0003$), indicating impaired working memory performance. Effect size difference in the time in the novel arm (%) across WT and 5xFAD groups for male (Cohen's D = -1.09) and female (Cohen's D = -2.88) mice. **d**, Mean ΔF/F trace during the 4 seconds prior to and following novel arm entry (T = 0). **e**, Area under the curve (AUC) of the ΔF/F trace during the second preceding novel arm entry. 5xFAD mice show a decreased AUC during this period (two-way ANOVA, effect of genotype, $F_{(23)} = 13.41$, $P = 0.001$), indicating reduced responsivity of PV-INs in 5xFAD mice to novel arm entry. Effect size difference in AUC across WT and 5xFAD groups for male (Cohen's D = -1.04) and female (Cohen's D = -1.75) mice. **f**, Mean ΔF/F trace during the 4 seconds prior to and following familiar arm entry (0). **g**, Area under the curve (AUC) of the ΔF/F trace during the second preceding familiar arm entry. 5xFAD mice show a decreased AUC during this period (two-way ANOVA, effect of genotype, $F_{(24)} = 4.378$, $P = 0.047$), indicating reduced responsivity of PV-INs in 5xFAD mice to familiar arm entry. Effect size difference in AUC across WT and 5xFAD groups for male (Cohen's D = -0.381) and female (Cohen's D = -1.36) mice. Scale bars represent 1 mm. Data represent mean ± SEM. $^*P < 0.05$. All statistical comparisons have been provided as a Stats Table file.

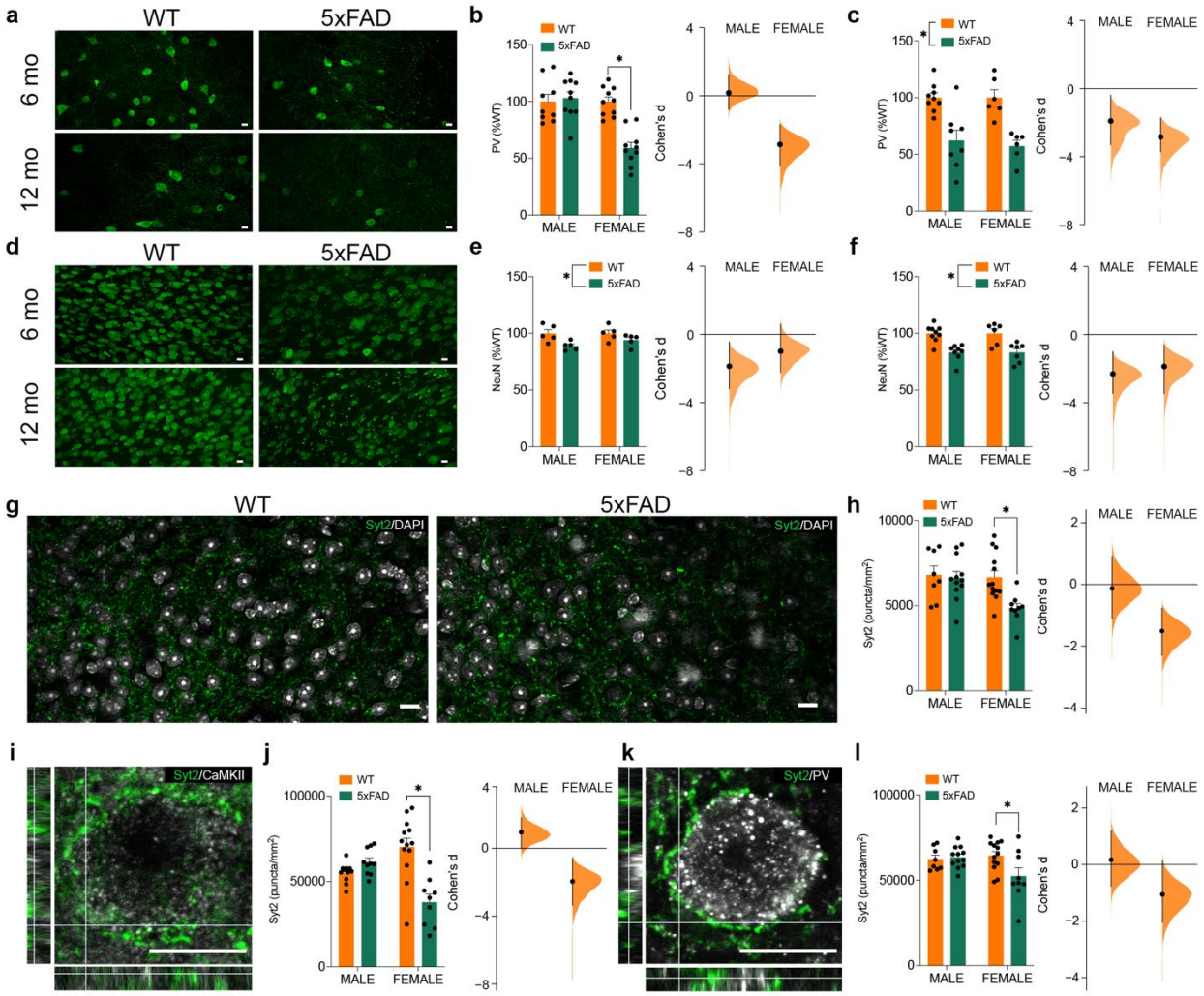


**Fig. 4: Immunohistochemical changes in the expression of PV-INs in the RSC.**

**a**, PV staining in the RSC of 6- and 12-month-old WT and 5xFAD mice. **b**, PV-IN counts in the RSC of 6-month-old 5xFAD mice as a percentage of the mean of each WT group. Female 5xFAD mice show a decrease in RSC PV-INs (two-way ANOVA, Sex X Genotype interaction, $F_{(35)} = 9.584$, $P = 0.003$; Tukey's test, Female WT vs. Female 5xFAD, $P = 0.0019$). Effect size difference between WT and 5xFAD groups for male (Cohen's D = 0.166) and female (Cohen's D = -2.86) mice. **c**, PV-IN counts in the RSC of 12-month-old 5xFAD mice as a percentage of the mean of each WT group. 5xFAD mice show a decrease in RSC PV-INs (two-way ANOVA, effect of genotype, $F_{(25)} = 25.70$, $P < 0.0001$). Effect size difference between WT and 5xFAD groups for male (Cohen's D = -1.91) and female (Cohen's D = -2.84) mice. **d**, NeuN staining in the RSC of 6-month-old and 12-month-old WT and 5xFAD mice. **e**, NeuN counts in the RSC of 6-month-old 5xFAD mice as a percentage of each WT group. 5xFAD mice showed decreased RSC NeuN density (two-way ANOVA, effect of genotype, $F_{(16)} = 10.27$, $P = 0.005$). Effect size difference between WT and 5xFAD groups for male (Cohen's D = -1.87) and female (Cohen's D = -0.994) mice. **f**, NeuN counts in the RSC of 12-month-old 5xFAD mice as a percentage of the mean of each WT group. 5xFAD mice showed decreased NeuN labeling (two-way ANOVA, effect of genotype, $F_{(26)} = 32.09$, $P < 0.0001$), indicating significant loss of neurons in these mice. Effect size difference between WT and 5xFAD groups

for male (Cohen's D = -2.31) and female (Cohen's D = -1.88) mice. **g**, Representative photomicrographs of Synaptophysin2 (Syt2; green) and DAPI (greyscale) staining in WT and 5xFAD mice. **h**, Density of Syt2 puncta (puncta/mm$^2$) in WT and 5xFAD mice. Female 5xFAD mice showed reduced Syt2 puncta (two-way ANOVA, Sex X Genotype interaction, $F_{(38)} = 4.165$, $P = 0.048$; Tukey's test, Female WT vs. Female 5xFAD, $P = 0.0111$). Effect size difference in the density of Syt2 puncta between WT and 5xFAD groups for male (Cohen's D = -0.134) and female (Cohen's D = -1.51) mice. **i**, Representative photomicrographs of Syt2 (green) and CaMKII (greyscale) staining. **j**, Density of Syt2 puncta (puncta/mm$^2$) on CaMKII$^+$ cells in WT and 5xFAD mice. Female 5xFAD mice showed a reduced density of Syt2 puncta (two-way ANOVA, Sex X Genotype interaction, $F_{(39)} = 24.28$, $P = 0.021$; test, Female WT vs. Female 5xFAD, $P < 0.0001$. Effect size difference of Syt2 puncta on CaMKII$^+$ cells between WT and 5xFAD groups for male (Cohen's D = 0.962) and female (Cohen's D = -1.95) mice. **k**, Representative photomicrographs of Syt2 (green) and PV (greyscale) staining **l**, Density of Syt2 puncta (puncta/mm$^2$) on PV$^+$ cells in WT and 5xFAD mice. Female 5xFAD mice showed a reduced density of Syt2 puncta (two-way ANOVA, Sex X Genotype interaction, $F_{(38)} = 4.953$, $P = 0.032$; Tukey's test, Female WT vs. Female 5xFAD, $P = 0.0254$). Effect size difference in Syt2 puncta on PV$^+$ cells between WT and 5xFAD groups for male (Cohen's D = 0.167) and female (Cohen's D = -1.06) mice. Scale bars represent 10 μm. Data represent mean ± SEM. $^*P < 0.05$. All statistical comparisons have been provided as a Stats Table file.

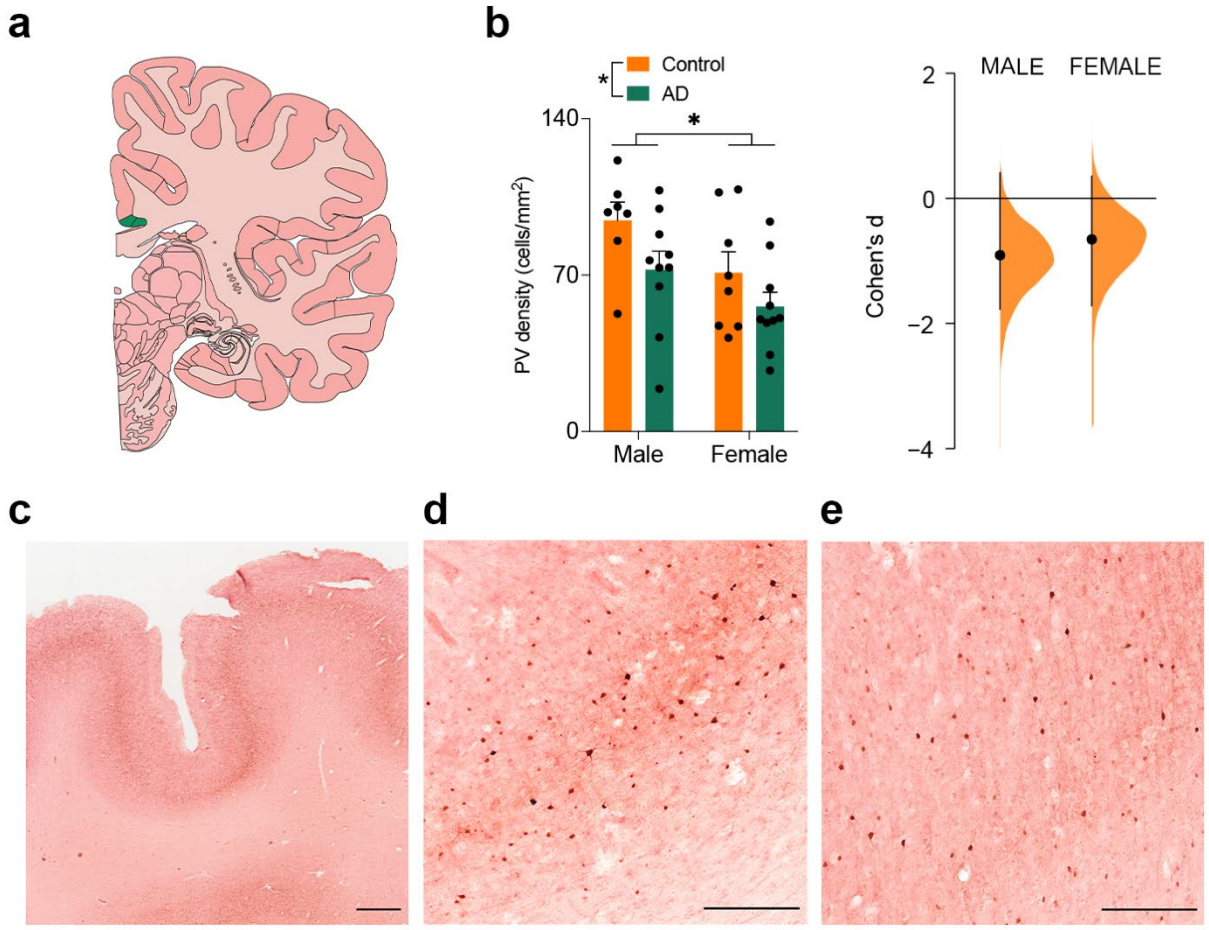


**Fig. 5: Sex and Alzheimer's disease contribute to the density of RSC PV-INs in post-mortem human tissue samples.**

**a**, Schematic illustrating the location of the retrosplenial cortex (BA 29 & 30) within a coronal plane of the Allen Human Brain Reference Atlas. **b**, Density (cells/mm$^2$) of RSC PV-INs in post-mortem brain samples obtained from male and female controls and AD patients. Overall, females had lower densities of RSC PV-INs compared to males (two-way ANOVA, effect of sex, $F_{(31)}$ = 6.078, $P$ = 0.0194). AD patients also had lower RSC PV-IN densities compared to samples from controls (two-way ANOVA, effect of AD-status, $F_{(31)}$ = 5.250, $P$ = 0.0289. Effect size difference in RSC PV-IN density between control and AD groups for males (Cohen's D = -0.906) and females (Cohen's D = -0.654). **c**, Representative photomicrograph showing an overview (20X magnification) of PV staining in a sample of human RSC. Representative photomicrographs of PV staining in the RSC of (**d**) control and (**e**) AD patients (20X magnification). Scale bars represent 250 μm. Data represent mean ± SEM. *$P$ < 0.05. All statistical comparisons have been provided as a Stats Table file.

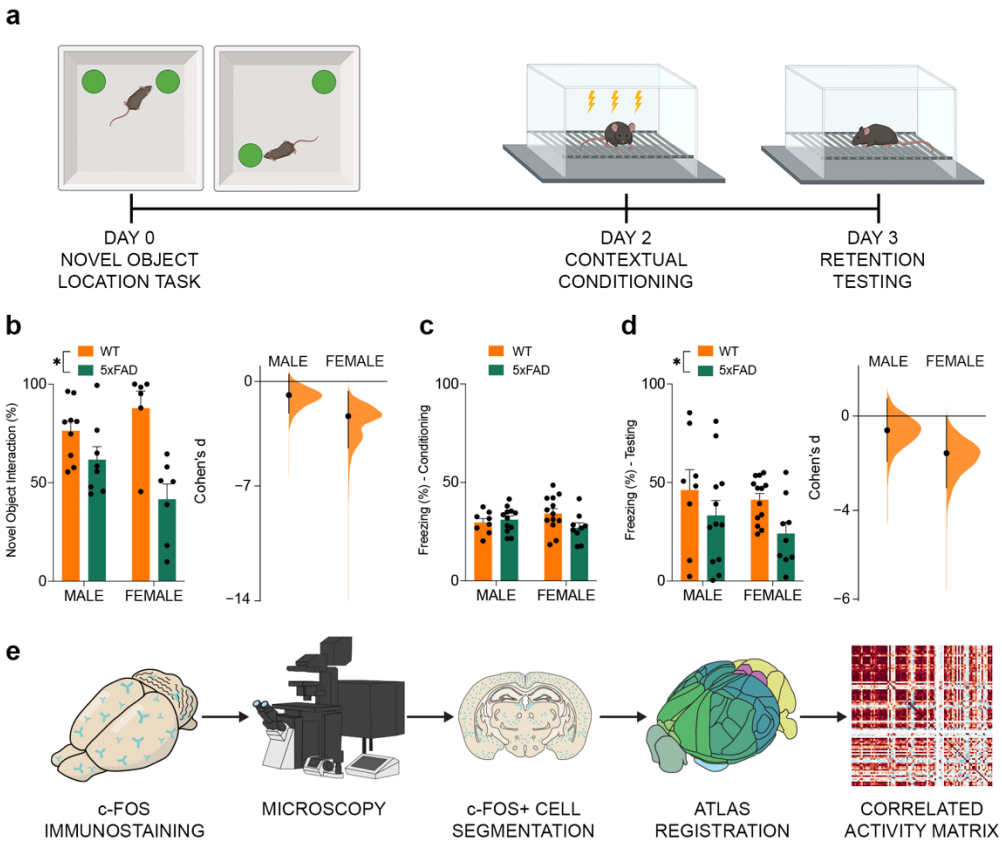

**Fig. 6: Altered functional connectivity of the RSC underlies cognitive impairments in female 5xFAD mice.**

**a**, Schematic outlining the timeline of behavioral testing. **b**, Time spent interacting with the object in the novel location, as a percentage of the total interaction time. 5xFAD mice spent less time interacting with the object in the novel location (two-way ANOVA, effect of genotype, $F_{(26)} = 19.65$, $P = 0.0002$). Effect size difference in the time spent freezing between WT and 5xFAD groups for male (Cohen's D = -0.877) and female (Cohen's D = -2.22) mice. **c**, Percentage of time spent freezing during contextual conditioning. **d**, Percentage of time spent freezing during retention testing. 5xFAD mice spent less time freezing upon context reintroduction (two-way ANOVA, effect of genotype, $F_{(38)} = 4.932$, $P = 0.0324$). Effect size difference the time spent freezing between WT and 5xFAD groups for male (Cohen's D = -0.469) and female (Cohen's D = -1.22) mice. **e**, Schematic outlining the generation of functional connectivity networks from brain-wide c-Fos staining. Circle plots outlining the functional connectome of the RSC in (**f**) female WT, (**g**) female 5xFAD, (**h**) male WT, and (**i**) male 5xFAD mice. Correlations with positive Pearson's correlation coefficients are depicted in black, while correlations with negative correlation coefficients (anti-correlations) are depicted in green. Line weight is indicative of the magnitude of the correlation coefficient. **j**, Number of anti-correlations involving the RSC in female WT and 5xFAD mice. **k**, Number of anti-correlations involving the RSC in male WT and 5xFAD mice. Data represent mean ± SEM. $^*P < 0.05$. All statistical comparisons have been provided as a Stats Table file.

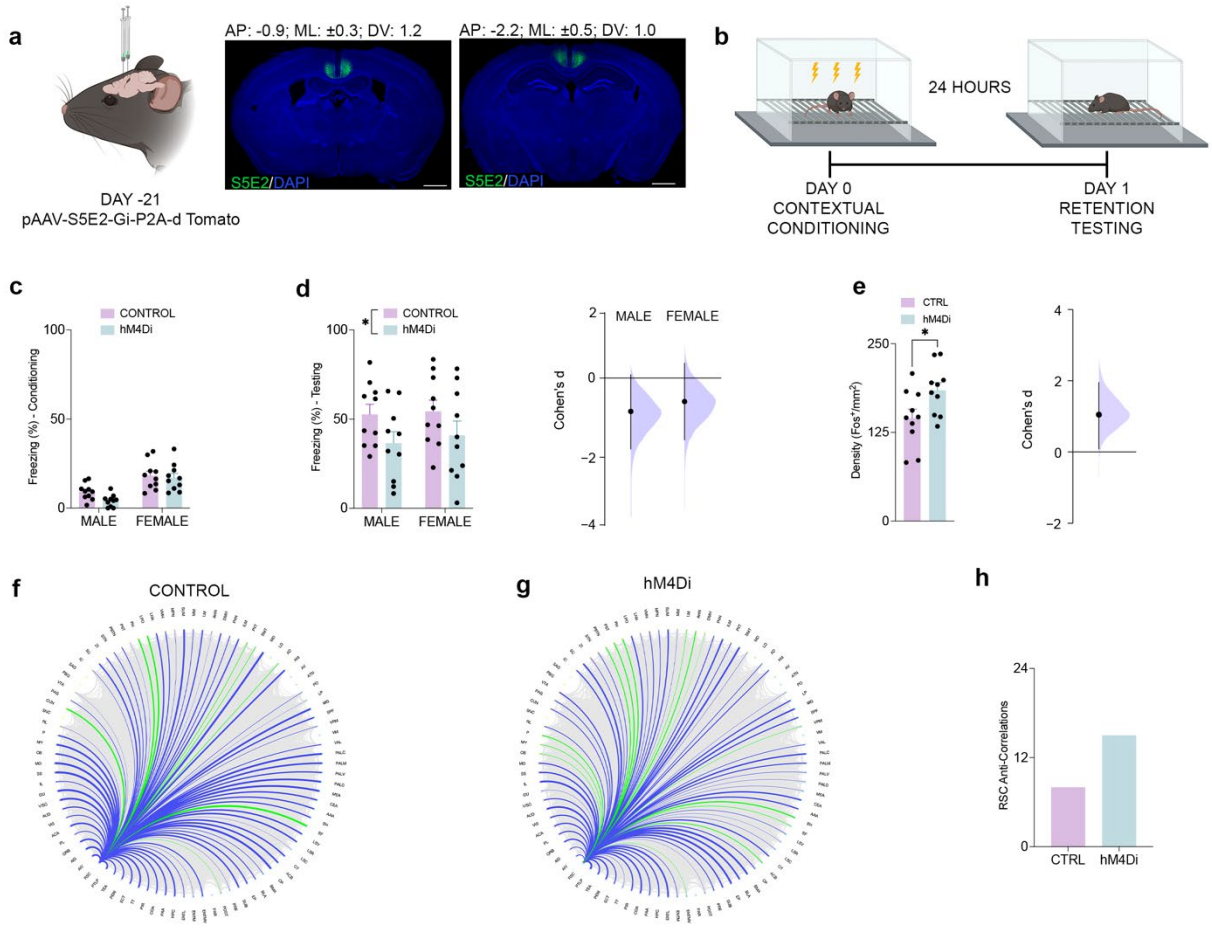


**Fig. 7: Targeted inhibition of RSC PV-INs in healthy mice mimics the impaired memory performance and RSC functional connectivity observed in 5xFAD mice.**

**a**, Schematic showing pAAV-S5E2-Gi-P2A-d Tomato (hM4Di) or pAAV-S5E2-GFP (control) virus injection site and representative photomicrographs of virus expression. **b**, Schematic outlining the contextual fear conditioning task. **c**, Percentage of time spent freezing during contextual conditioning. **d**, Percentage of time spent freezing during retention testing. Mice injected with hM4Di spent less time freezing upon context reintroduction (two-way ANOVA, effect of virus, $F_{(36)} = 4.993$, $P = 0.0317$). Effect size difference in the time spent freezing upon context reintroduction between control and hM4Di groups for male (Cohen's D = -0.844) and female (Cohen's D = -0.594) mice. (**e**) The expression density of c-Fos+ cells was increased in hM4Di mice (two-sample *t* test, $t_{(18)} = 2.343$, $P = 0.0308$) indicating hyperactivity. Effect size difference in c-Fos expression density across control and hM4Di groups (Cohen's D = 1.05). Circle plots outlining the functional connectome of the RSC in (**f**) control and (**g**) hM4Di mice. Correlations with positive Pearson's correlation coefficients are depicted in blue, while correlations with negative correlation coefficients (anti-correlations) are depicted in green. Line weight is indicative of the magnitude of the correlation coefficient. **h**, Number of anti-correlations involving the RSC in control and hM4di mice. Scale bars represent 1 mm. Data represent mean ± SEM. $^*P < 0.05$. All statistical comparisons have been provided as a Stats Table file.

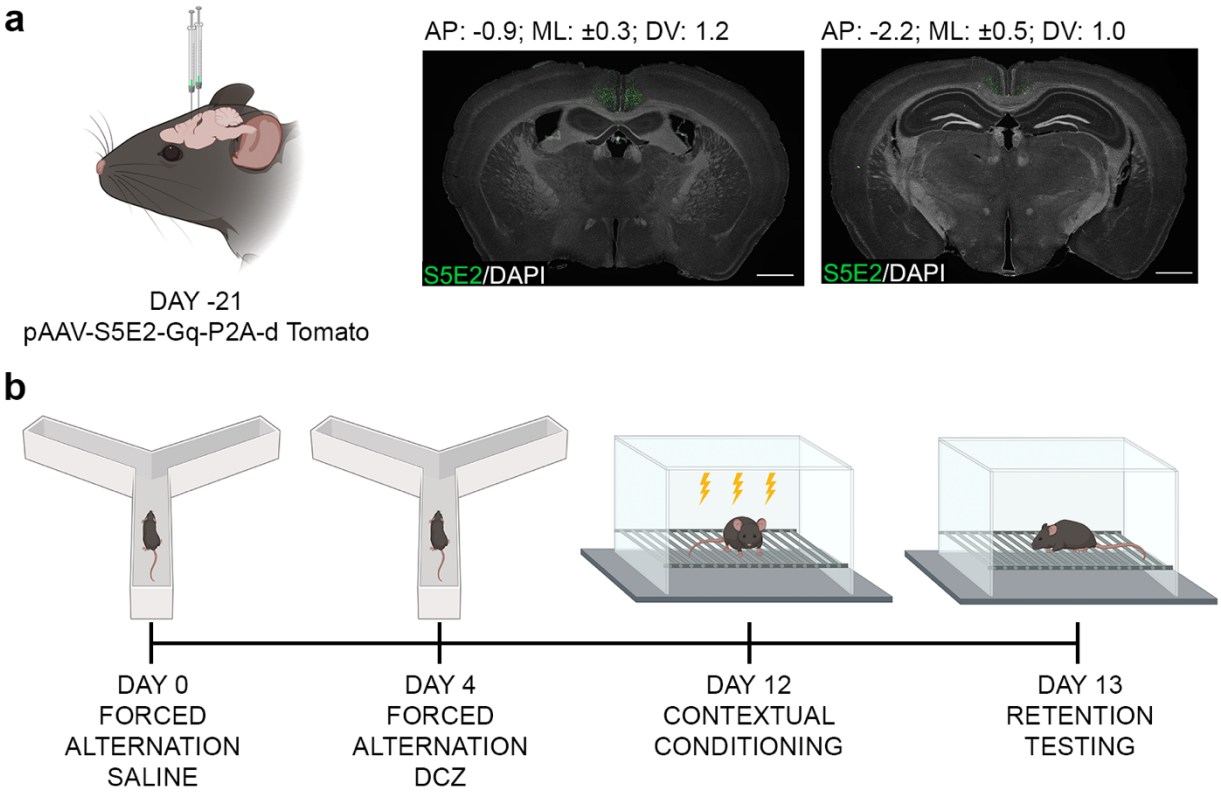

**Fig. 8: Stimulation of RSC PV-INs promotes the recovery of memory performance in 5xFAD mice.**

**a**, Schematic showing pAAV-S5E2-Gq-P2A-d Tomato (hM3Dq) virus injection site and representative photomicrographs of virus expression. **b**, Schematic outlining the behavioral testing schedule. **c**, Percentage of time spent in the novel arm of the forced alternation Y-maze task by male mice with saline treatment and subsequent DCZ treatment. **d**, Percentage of time spent in the novel arm of the forced alternation y maze task by female mice with saline treatment and subsequent DCZ treatment. Saline-treated female mice spent less time in the novel arm of this task (two-way repeated-measures ANOVA, effect of drug, $F_{(11)} = 5.881$, $P = 0.0337$), indicating improved working memory performance with DCZ treatment. Effect size difference in the time spent in the novel arm of the y maze task between saline and DCZ treatment for WT (Cohen's D = 0.363) and 5xFAD (Cohen's D = 1.27) mice. **e**, Activity suppression ratio during contextual fear condition for male WT and 5xFAD mice. **f**, Activity suppression ratio during contextual fear condition for female WT and 5xFAD mice. Saline-treated female 5xFAD mice displayed higher suppression ratios than DCZ-treated 5xFAD mice (two-way ANOVA, Genotype X Treatment interaction, $F_{(35)} = 4.115$, $P = 0.0731$; *a priori* two sample *t* test, 5xFAD saline vs. 5xFAD DCZ, $t_{(5)} = 4.163$, $P = 0.0088$), indicating improved contextual memory performance with DCZ treatment. Effect size difference in activity suppression between saline and DCZ treatment for WT (Cohen's D = -0.558) and 5xFAD (Cohen's D = -3.18) mice. Scale bars represent 1 mm. Data represent mean ± SEM. $^*P < 0.05$. All statistical comparisons have been provided as a Stats Table file.